Supplementary Information

23.2% efficient low band gap perovskite solar cells with cyanogen management

W. Hashini K. Perera[#], Thomas Webb[#], Yuliang Xu, Jingwei Zhu, Yundong Zhou, Gustavo F. Trindade, Mateus G. Masteghin, Steven P. Harvey, Sandra Jenatsch, Linjie Dai, Sanjayan Sathasivam, Thomas J. Macdonald, Steven J. Hinder, Yunlong Zhao, Samuel D. Stranks, Dewei Zhao, Wei Zhang, K. D. G. Imalka Jayawardena, Saif A. Haque*, and S. Ravi P. Silva**

Supplementary Table 1. Examples of reported work indicating the stability testing of SCN^- containing devices in an inert atmosphere.

Perovskite	Device Architecture	Condition	Ref
Pb perovskites			
$MAPbI_3$	ITO/PEDOT:PSS/Perovskite/PCBM/C60/LiF/Al	ISOS-D1I	1
$MAPbI_3$	ITO/PEDOT:PSS/Perovskite/PCBM/C60/LiF/Al		
$Cs_{0.1}FA_{0.9}PbBr_{2.1}I_{0.9}$	ITO/2PACz/Perovskite/C60/BCP/Ag	ISOS-D1I	2
$Cs_{0.1}FA_{0.9}PbBr_{2.1}I_{0.9}$ + MAI + KSCN	ITO/2PACz/Perovskite/C60/BCP/Ag		
Sn perovskites			
$FA_{0.75}MA_{0.25}SnI_2Br$	FTO/PEDOT:PSS/KSCN/Perovskite/ICBA/BPhen/Ag	ISOS-D1I	3
$FA_{0.75}MA_{0.25}SnI_2Br$	FTO/PEDOT:PSS/KSCN/Perovskite/ICBA/BPhen/Ag		
$PEA_{0.1}FA_{0.9}SnI_3$	ITO/PEDOT:PSS/Perovskite/PCBM/Al	ISOS-D1I	4
$PEA_{0.1}FA_{0.9}SnI_3$ + FASCN	ITO/PEDOT:PSS/Perovskite/PCBM/Al		
$FASnI_3$	ITO/PEDOT:PSS/Perovskite/PCBM/Ag	ISOS-L1I	5
$FASnI_3$+PEASCN	ITO/PEDOT:PSS/Perovskite/PCBM/Ag		
Pb-Sn mixed perovskites			
$FA_{0.7}MA_{0.3}Pb_{0.7}Sn_{0.3}I_3$	ITO/PEDOT:PSS/Perovskite/PCBM/C60/BCP/Ag	ISOS-D1I	6
$FA_{0.7}MA_{0.3}Pb_{0.7}Sn_{0.3}I_3$ + NH_4SCN	ITO/PEDOT:PSS/Perovskite/PCBM/C60/BCP/Ag		
$Cs_{0.1}FA_{0.6}MA_{0.3}Pb_{0.5}Sn_{0.5}I_3$ + NH_4SCN	ITO/PEDOT:PSS/Perovskite/C60/BCP/Ag	ISOS-D1I	7
$Cs_{0.1}FA_{0.6}MA_{0.3}Pb_{0.5}Sn_{0.5}I_3$ + NH_4SCN	ITO/PEDOT:PSS/Perovskite/$EDAI_2$/C60/BCP/Ag		
$Cs_{0.1}FA_{0.6}MA_{0.3}Pb_{0.5}Sn_{0.5}I_3$ + NH_4SCN +GASCN	ITO/PEDOT:PSS/Perovskite/$EDAI_2$/C60/BCP/Ag		
$Cs_{0.05}FA_{0.85}MA_{0.1}Pb_{0.5}Sn_{0.5}I_3$ + MASCN + PySCN	ITO/PEDOT:PSS/Perovskite/C60/BCP/Ag	ISOS-D1I	8
$FA_{0.6}MA_{0.4}Pb_{0.4}Sn_{0.6}I_3$ + GASCN + PEAI	ITO/PEDOT:PSS/Perovskite/C60/BCP/Ag	ISOS-L1I	9
$FA_{0.6}MA_{0.4}Pb_{0.4}Sn_{0.6}I_3$ + $Pb(SCN)_2$	ITO/PEDOT:PSS/Perovskite/C60/BCP/Ag	ISOS-D1I	10
$FA_{0.7}MA_{0.3}Pb_{0.5}Sn_{0.5}I_3$ + NH_4SCN + GlyHCl	ITO/PEDOT:PSS/Perovskite/C60/BCP/Cu	ISOS-D1I	11
$FA_{0.7}MA_{0.3}Pb_{0.5}Sn_{0.5}I_3$ + NH_4SCN + GlyHCl+SnO_x	ITO/PEDOT:PSS/Perovskite/C60/BCP/Cu		
$Cs_{0.1}FA_{0.6}MA_{0.3}Pb_{0.5}Sn_{0.5}I_3$ + NH_4SCN + GlyHCl	ITO/PEDOT:PSS/Perovskite/C60/BCP/Ag	ISOS-D1I	12
$Cs_{0.1}FA_{0.6}MA_{0.3}Pb_{0.5}Sn_{0.5}I_3$ + NH_4SCN + GlyHCl	ITO/PEDOT:PSS/Perovskite/PP/C60/BCP/Ag		
$Cs_{0.1}FA_{0.6}MA_{0.3}Pb_{0.5}Sn_{0.5}I_3$ + NH_4SCN + GlyHCl	ITO/PEDOT:PSS/Perovskite/PPCPTA/C60/BCP/Ag		
$FA_{0.5}MA_{0.5}Pb_{0.5}Sn_{0.5}I_3$+$Pb(SCN)_2$	ITO/PEDOT:PSS/Perovskite/PCBM/BCP/Ag	ISOS-D1I and ISOS-L1I	13
$FA_{0.5}MA_{0.5}Pb_{0.5}Sn_{0.5}I_3$+$Pb(SCN)_2$ + DOPA	ITO/PEDOT:PSS/Perovskite/PCBM/BCP/Ag		
$FAPb_{0.5}Sn_{0.5}I_3$ + KSCN	ITO/PEDOT:PSS/Perovskite/C60/BCP/Ag		

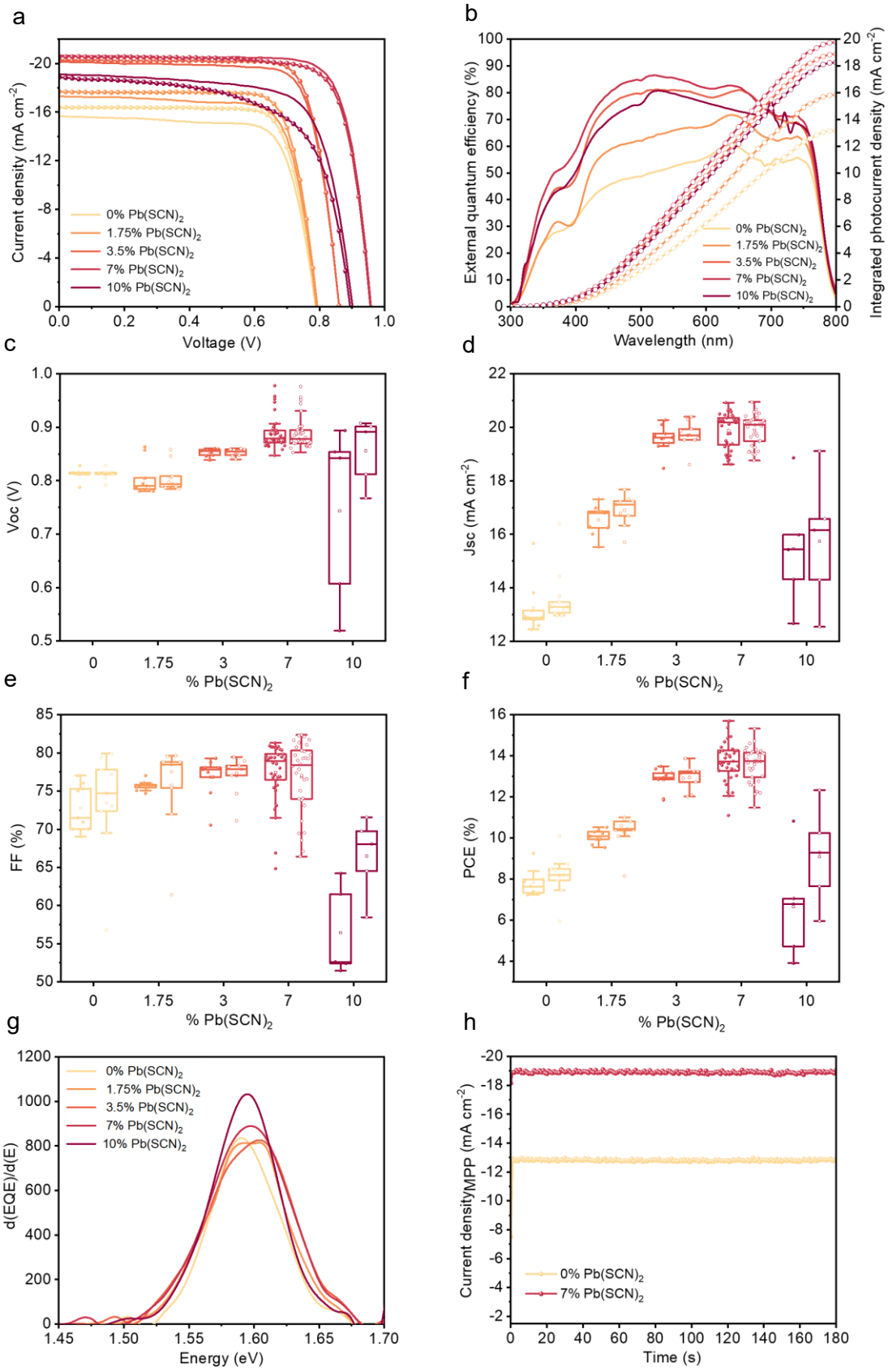

Supplementary Fig. 1. Optimisation of PEDOT:PSS/MAPI devices incorporating $Pb(SCN)_2$ as an additive to MAPI. **a**, *J-V* curves of champion devices in both forward (line) and reverse (line + symbol) directions. **b**, Corresponding EQE spectra and integrated J_{SC}. Box plots for **c**, V_{OC}, **d**, J_{SC} **e**, FF, and **f**, PCE. **g**, Differential of EQE. **h**, Stability of the photocurrent at maximum power point as determined from J-V scans.

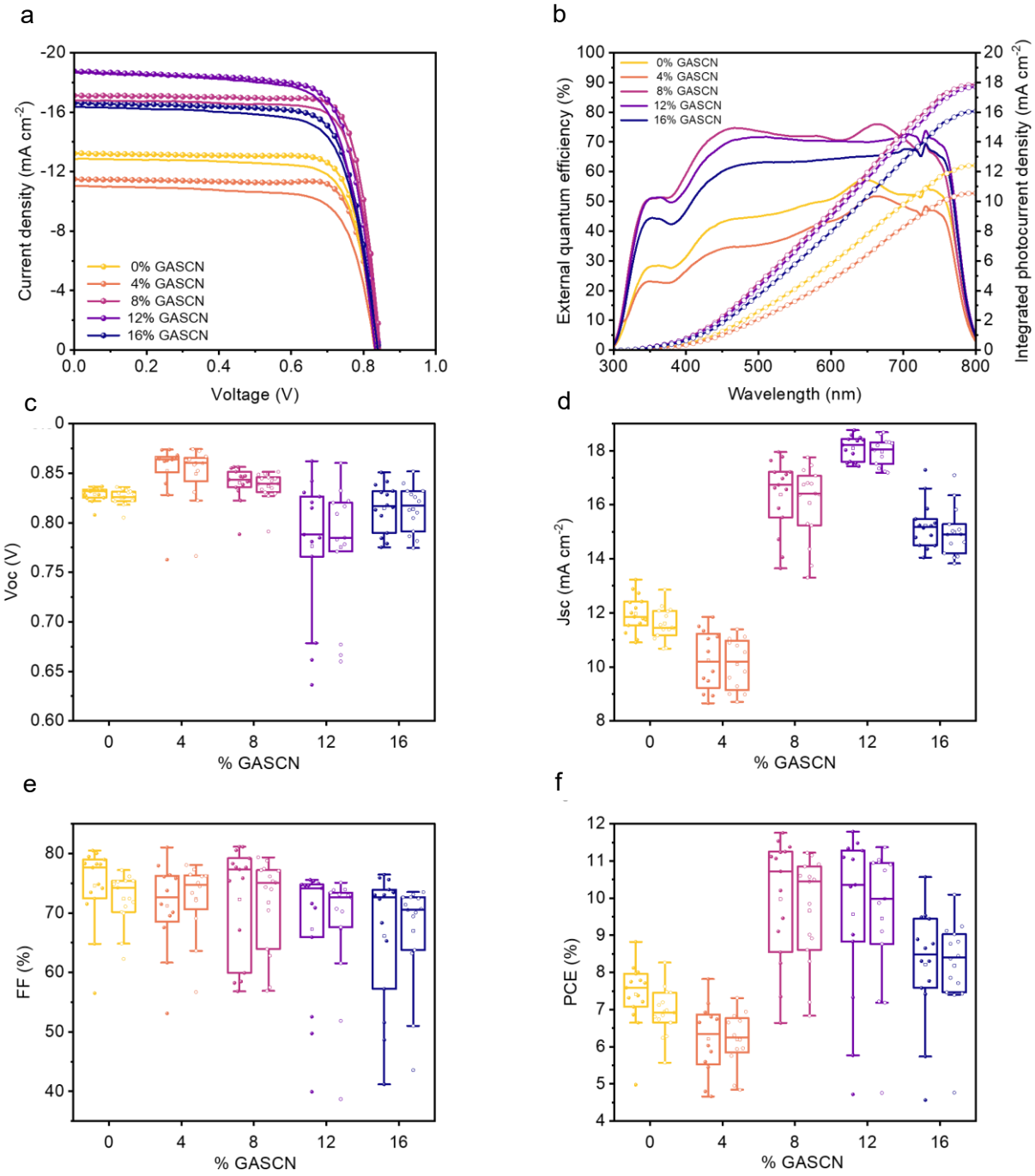

Supplementary Fig. 2. Optimisation of PEDOT:PSS/MAPI devices incorporating GASCN as an additive to MAPI. **a**, J-V curves of champion devices in both forward (line) and reverse (line + symbol) directions. **b**, Corresponding EQE spectra and integrated J_{SC}. Box plots for **c**, V_{OC}, **d**, J_{SC}, **e**, FF, and **f**, PCE.

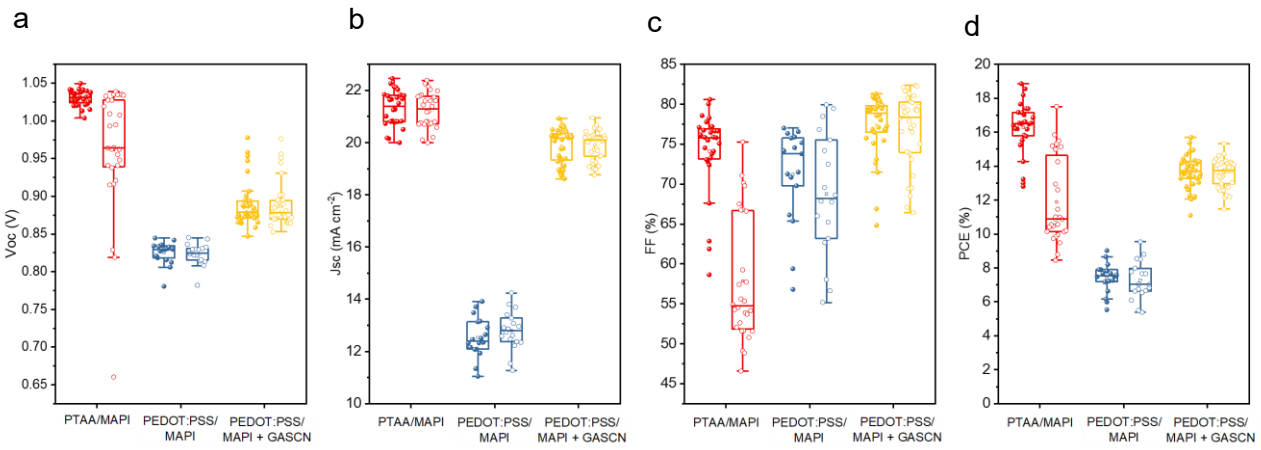

Supplementary Fig. 3. Statistical distribution of photovoltaic parameters for devices based on PTAA/MAPI, PEDOT:PSS/MAPI, and PEDOT:PSS/MAPI+GASCN. Box plots for **a**, V_{OC}, **b**, J_{SC}, **c**, FF, and **d**, PCE.

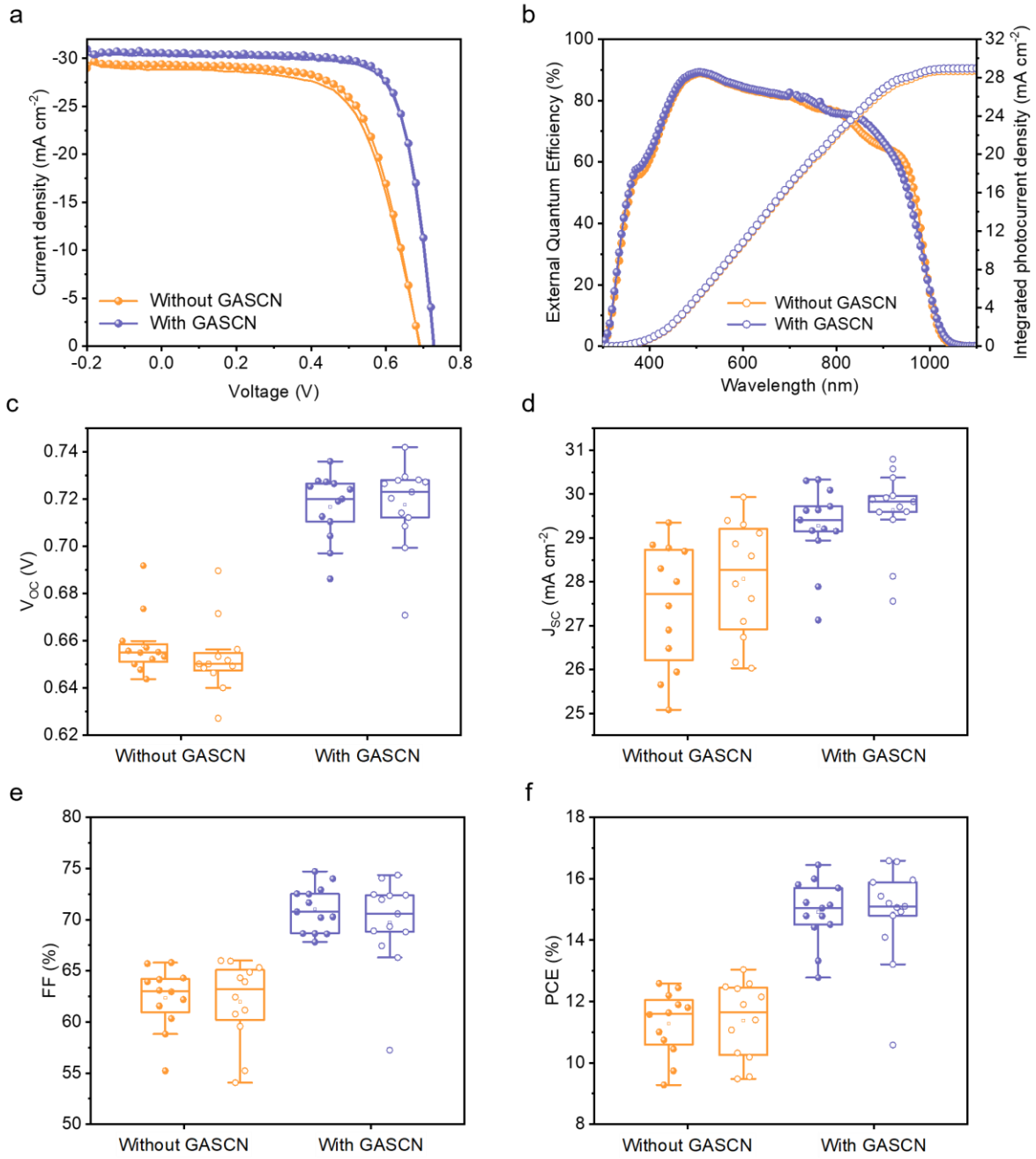

Supplementary Fig. 4. Device performance characteristics of PEDOT:PSS/$Cs_{0.1}FA_{0.6}MA_{0.3}Pb_{0.5}Sn_{0.5}I_3$ devices without and with GASCN as an additive. **a**, J-V curves of champion devices in both forward (line) and reverse (line + symbol) directions. **b**, Corresponding EQE spectra and integrated J_{SC}. Box plots for **c**, V_{OC}, **d**, J_{SC}, **e**, FF, and **f**, PCE.

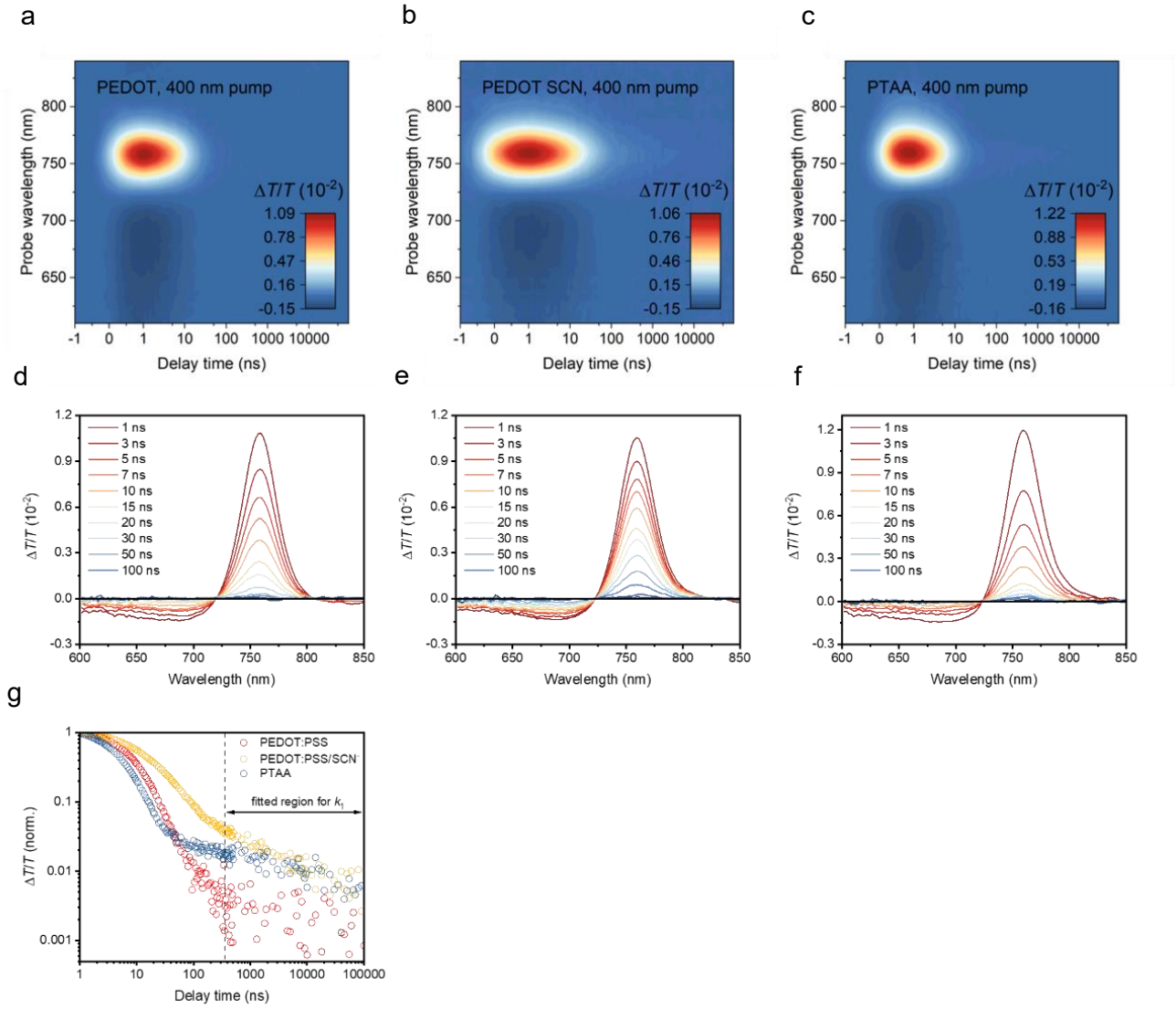

Supplementary Fig. 5. Transient absorption (TA) characterisation. TA maps of **a**, PEDOT:PSS, **b**, PEDOT:PSS/MAPI with $Pb(SCN)_2$, and **c**, PTAA/MAPI under a 3.1-eV pump. **d** – **f**, TA spectra of the above HTL/perovskites samples. **g**, Normalised kinetics of the Ground State Bleach for the HTL/perovskites samples.

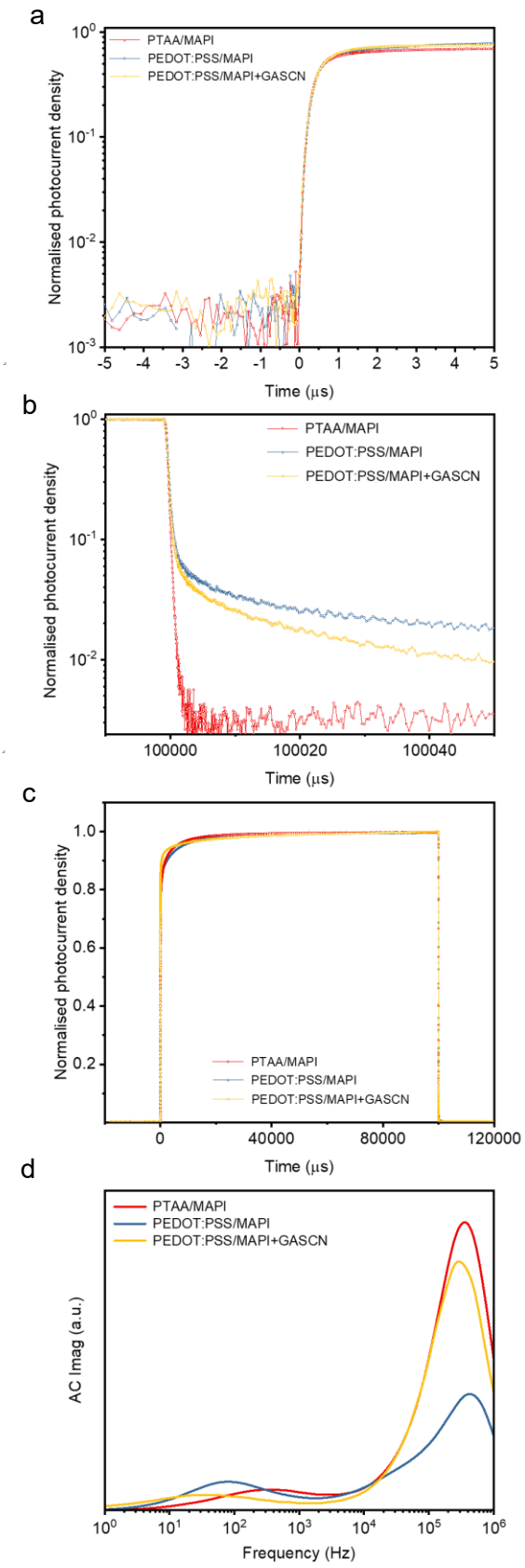

Supplementary Fig. 6. Time and frequency domain characterisation. **a**, Rise time, **b**, decay time and **c**, overall transient characteristics for PTAA/MAPI, PEDOT:PSS/MAPI, and PEDOT:PSS/MAPI + GASCN. **d**, IMPS spectra for the above devices.

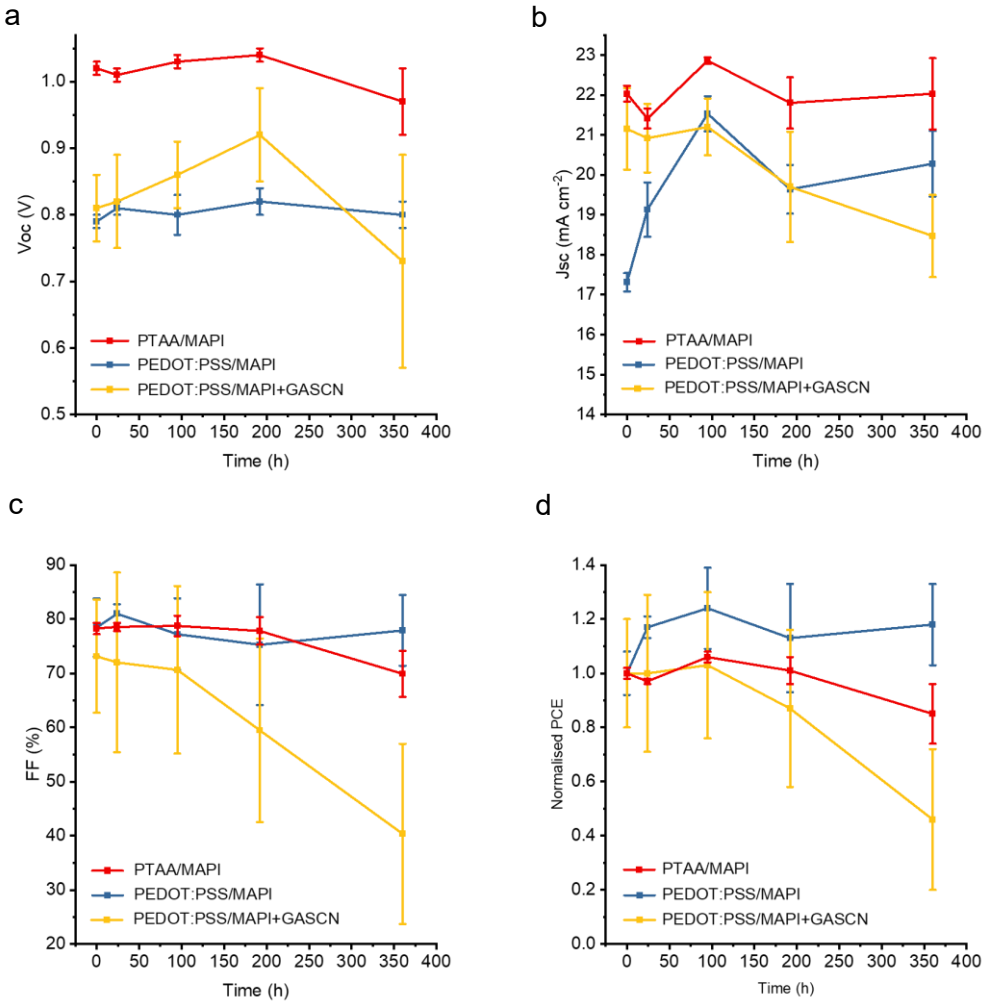

Supplementary Fig. 7. Changes to device performance parameters under ISOS-D1 at 65% relative humidity. **a**, V_{OC}, **b**, J_{SC}, **c**, FF, and **d**, Normalised PCE.

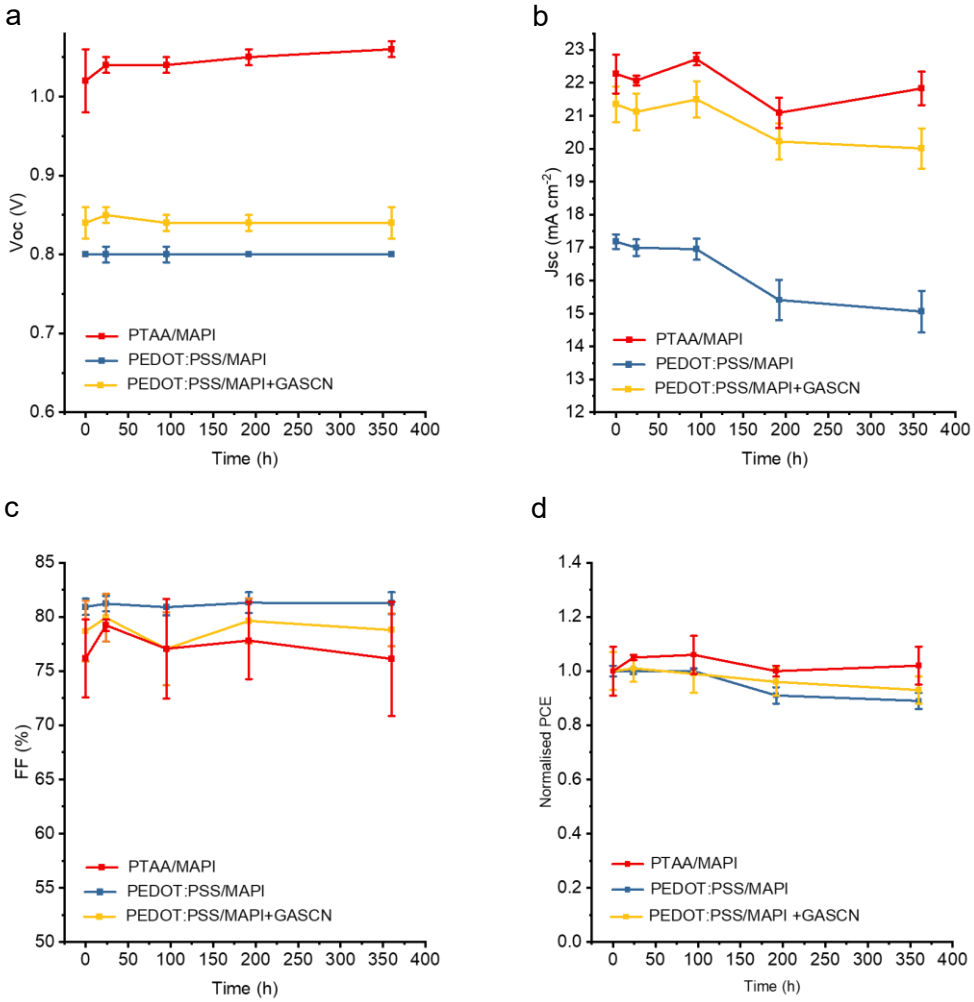

Supplementary Fig. 8. Changes to device performance parameters under ISOS-D1-I in a N_2 glove box. **a**, V_{OC}, **b**, J_{SC}, **c**, FF, and **d**, Normalised PCE.

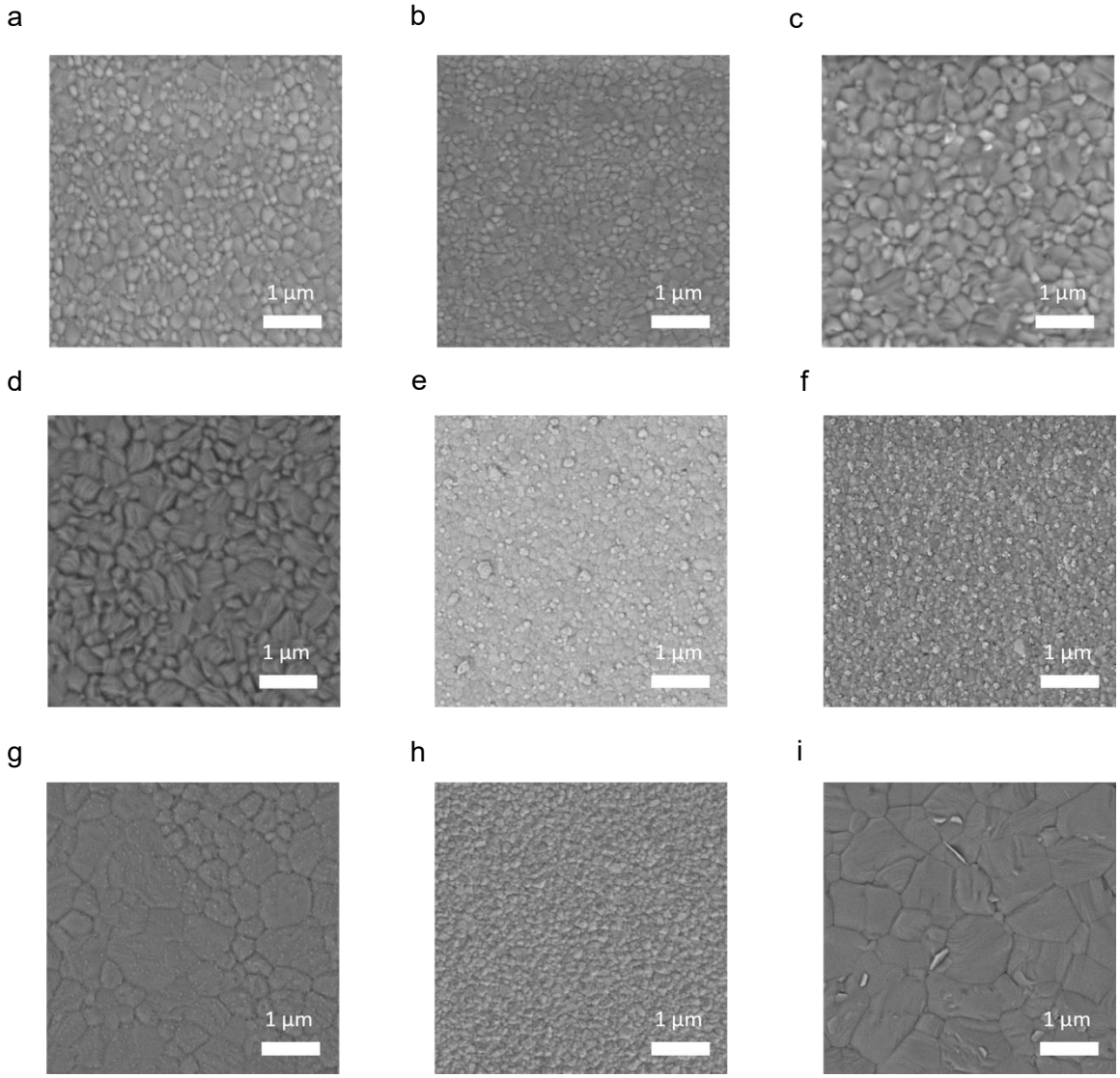

Supplementary Fig. 9. Microstructural changes under ISOS-D1 stability testing (SEM images). **a**–**c**, Fresh samples: **a**, PTAA/MAPI, **b**, PEDOT:PSS/MAPI, and **c**, PEDOT:PSS/MAPI + GASCN. **d**–**f**, Samples degraded for 2 weeks at 65% relative humidity: **d** PTAA/MAPI, **e**, PEDOT:PSS/MAPI, and **f**, PEDOT:PSS/MAPI + GASCN. **g**–**i,** Samples stored for 2 weeks in a N_2 glove box: **g**, PTAA/MAPI, **h**, PEDOT:PSS/MAPI, and **i**, PEDOT:PSS/MAPI + GASCN.

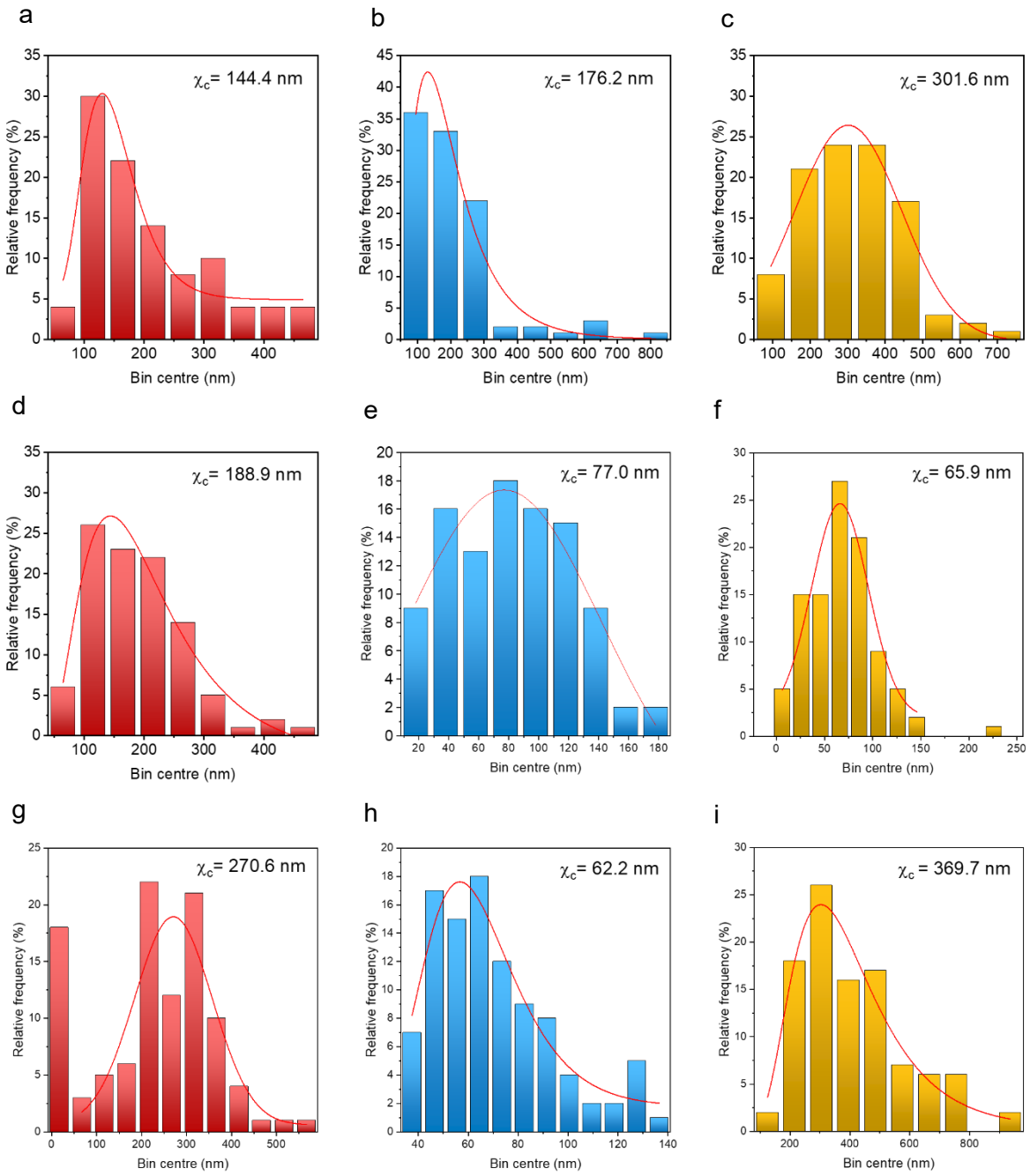

Supplementary Fig. 10. Microstructural changes under ISOS-D1 stability testing (grain size analysis). **a**-**c**, Fresh samples: **a**, PTAA/MAPI, **b**, PEDOT:PSS/MAPI, and **c**, PEDOT:PSS/MAPI + GASCN. **d** – **f** Samples degraded for 2 weeks at 65% relative humidity: **d**, PTAA/MAPI, **e**, PEDOT:PSS/MAPI, and **f**, PEDOT:PSS/MAPI + GASCN. **g**–**i**, Samples stored for 2 weeks in a N_2 glove box: **g**, PTAA/MAPI, **h**, PEDOT:PSS/MAPI, and **i**, PEDOT:PSS/MAPI + GASCN.

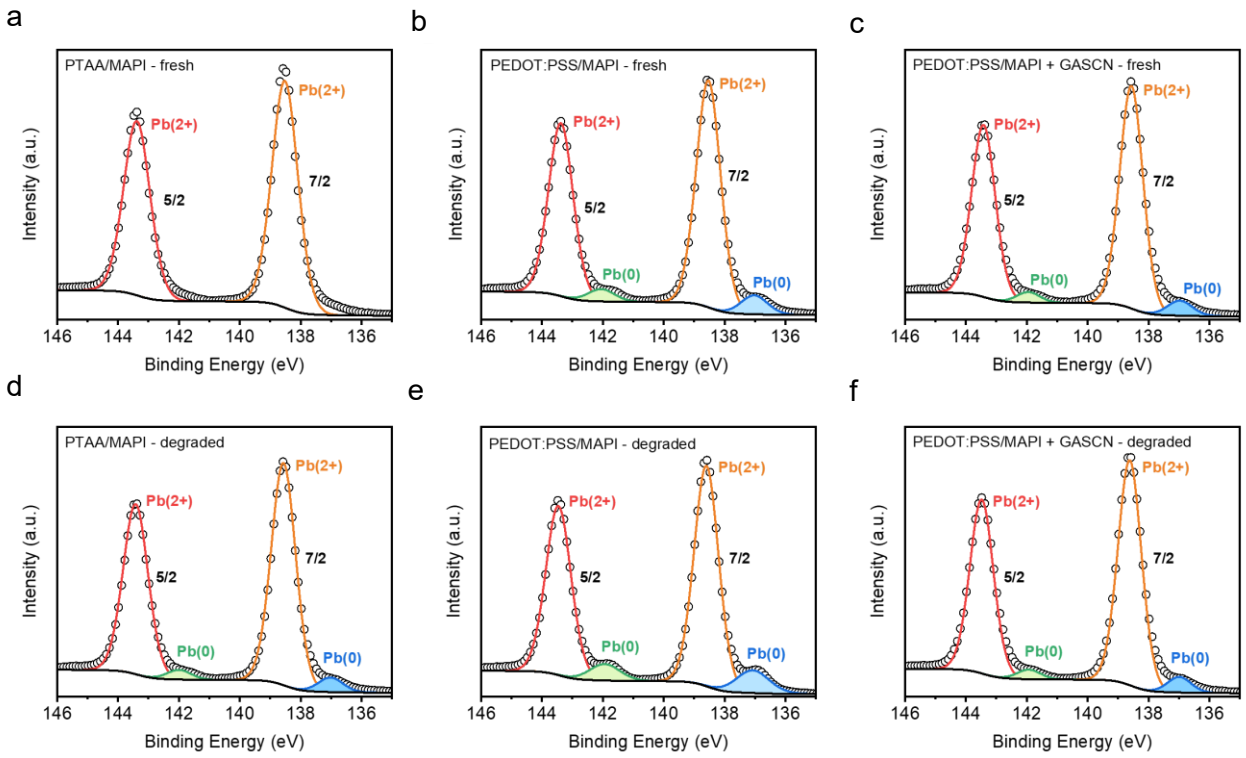

Supplementary Fig. 11. Surface composition change analysed using X-ray photoelectron spectroscopy. **a**–**c**, Fresh samples: **a**, PTAA/MAPI, **b**, PEDOT:PSS/MAPI, and **c**, PEDOT:PSS/MAPI + GASCN. **d**–**f**, Samples degraded for 2 weeks at 65% relative humidity: **d**, PTAA/MAPI, **e**, PEDOT:PSS/MAPI, and **f**, PEDOT:PSS/MAPI + GASCN.

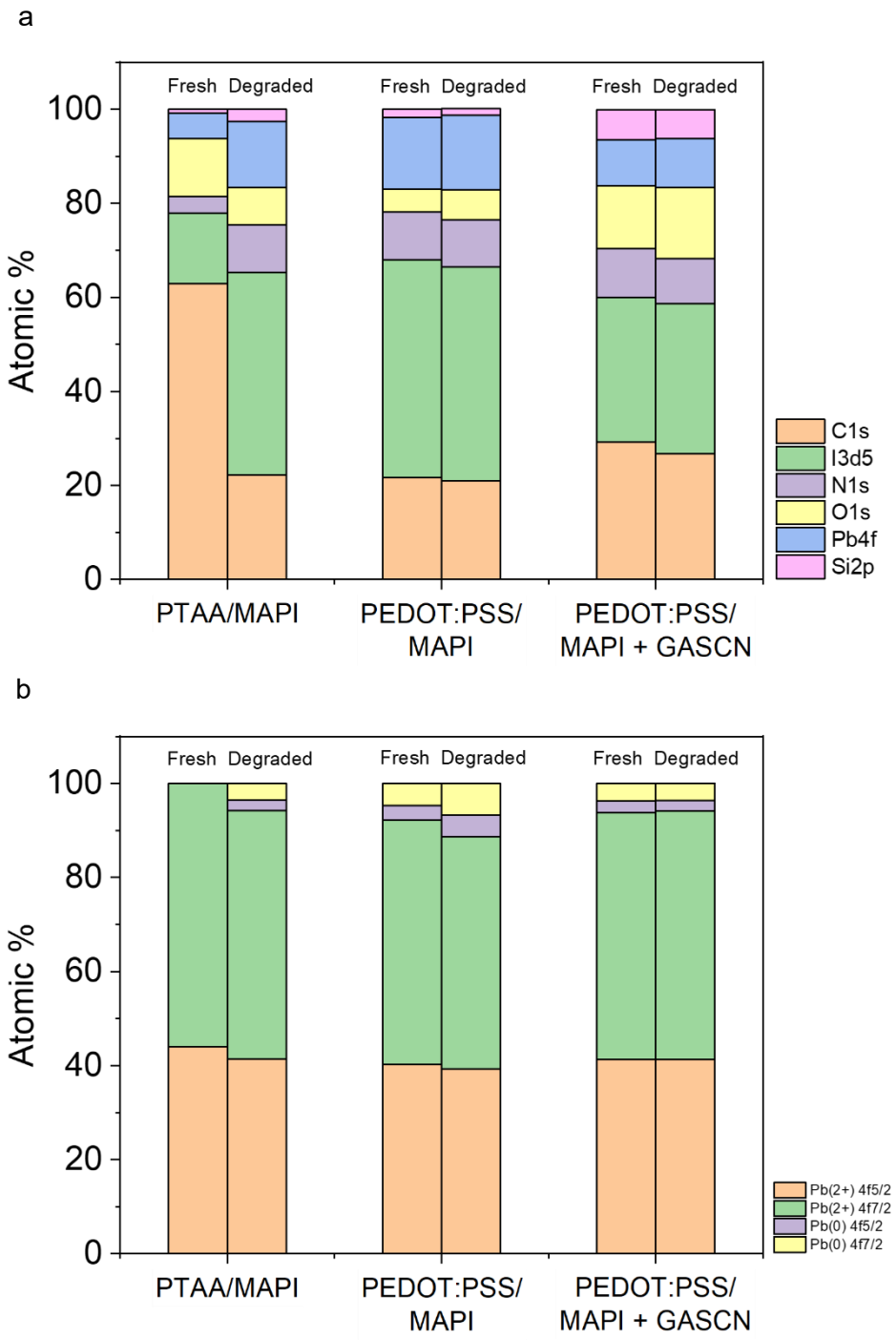

Supplementary Fig. 12. Surface composition change analysed using X-ray photoelectron spectroscopy. **a**, C 1s, I 3d, N 1s, O 1s, Pb 4f and Si 2p analysis. **b**, Pb 4f analysis, for fresh and degraded samples (for 2 weeks) of PTAA/MAPI, PEDOT:PSS/MAPI, and PEDOT:PSS/MAPI + GASCN.

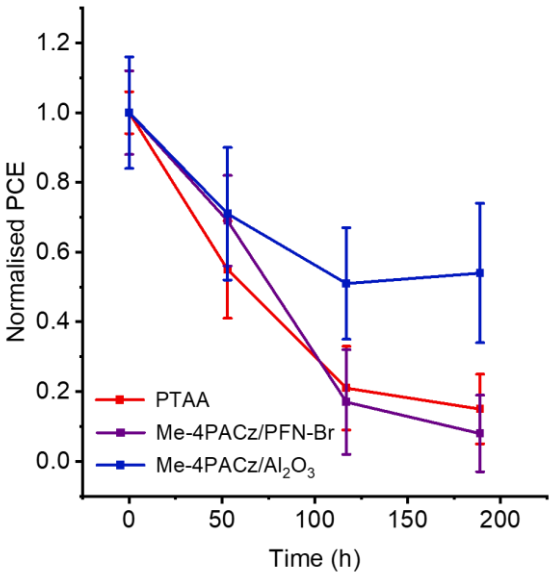

Supplementary Fig. 13. Variation of normalised PCE for devices based on PTAA and Me-4PACz containing SCN^- under ISOS-D-1 at 65% relative humidity.

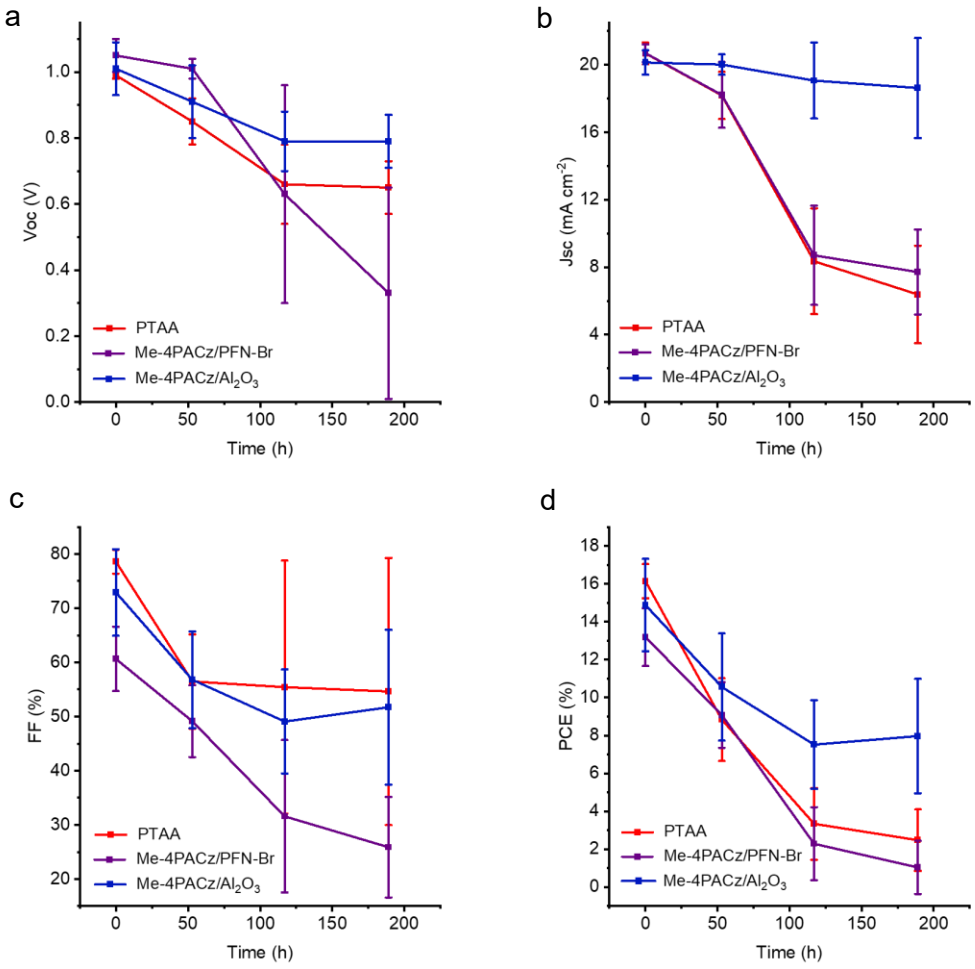

Supplementary Fig. 14. Changes to PTAA and Me-4PACz based device performance parameters under ISOS-D-1 at 65% relative humidity. **a**, V_{OC}, **b**, J_{SC}, **c**, FF, and **d**, PCE.

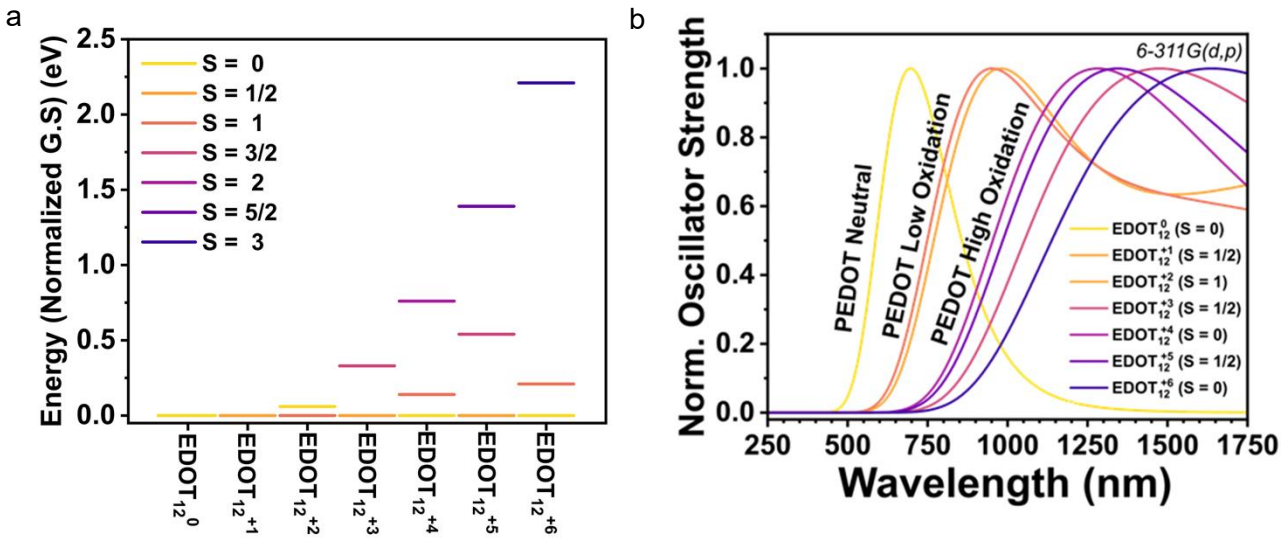

Supplementary Fig. 15. a, Comparison of the difference in ground state energies for different multiplicities of a 12-monomer PEDOT chain ($EDOT_{12}$) from Q = 0 to Q= +6 (50 % oxidation of the PEDOT chain). DFT calculations were performed using uB3LYP with a *6-311G*(d,p) functionals with Grimme's dispersion and following geometric optimisation using the same parameters. Assignments to optical transitions were confirmed by calculating the configuration interaction coefficients. **b**, Prediction of the normalised oscillator strength of the lowest energy ground-state for each oxidation which allows for prediction of the absorbance spectra. The predicted spectra indicate a greater degree of oxidation of the PEDOT chain leads to near-IR absorbance. At wavelengths of 830-850 nm we predict a distinct peak which can be attributed to the presence of lower oxidation of the PEDOT polymers (total oxidation < 17%). A lower wavelength peak at 650 nm was also observed which we our model attributes to the absorbance of neutral PEDOT.

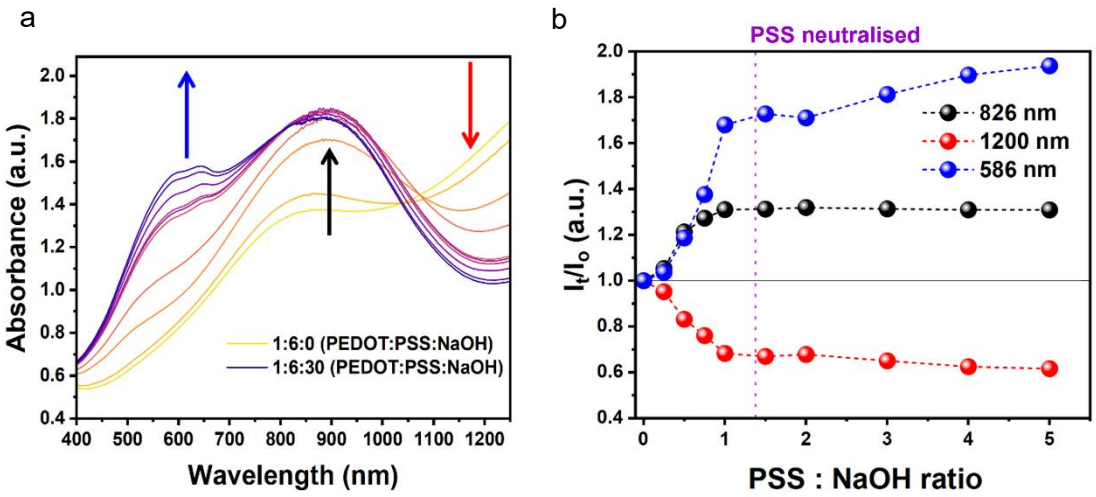

Supplementary Fig. 16 PEDOT:PSS de-doping phenomena upon addition of NaOH**,** UV-Visible absorbance spectra of PEDOT:PSS solution upon addition of increasing concentrations of NaOH revealing lowering of the PEDOT oxidation state and consequent de-doping phenomena. **a**, Full UV-Visible absorbance spectra, and **b**, Change in intensity of absorbance at 586 nm (neutral PEDOT), 826 nm (low oxidation PEDOT), and at NIR 1200 nm (higher oxidation states of PEDOT).

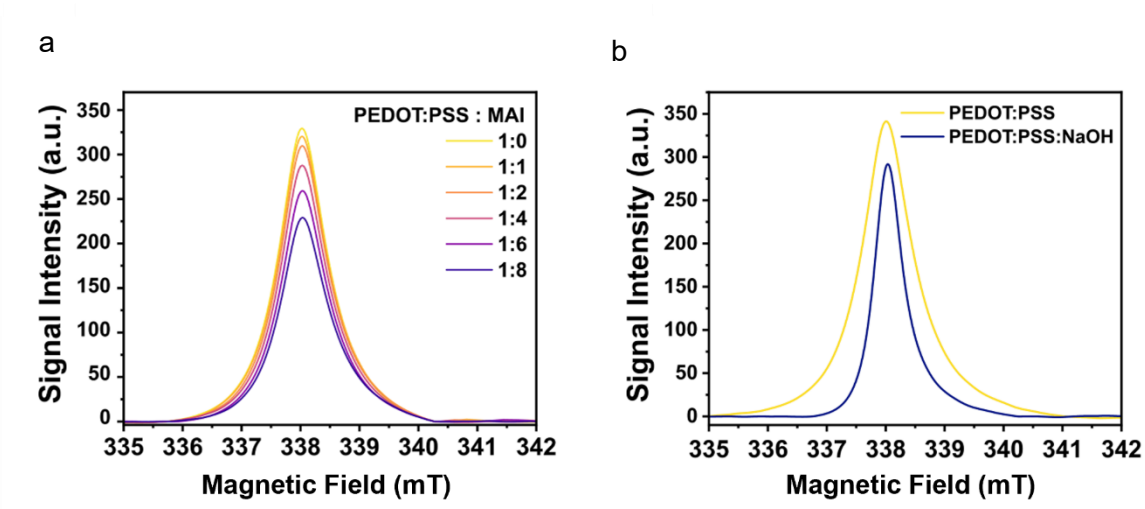

Supplementary Fig. 17. Electron Paramagnetic Resonance (EPR) spectroscopy of PEDOT:PSS when combined with **a**, methylammonium iodide and **b**, sodium hydroxide (PSS:NaOH - 1:1.5).

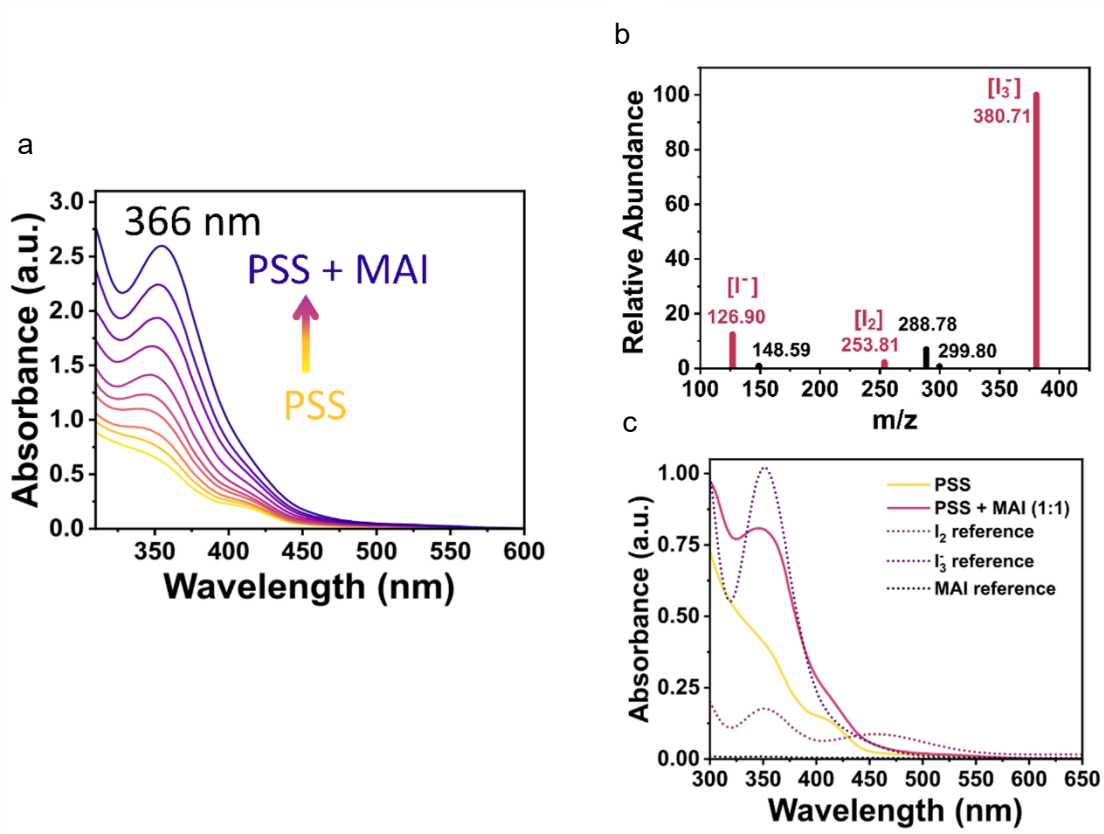

Supplementary Fig. 18. Investigating the mechanism of MAI-induced de-doping of PEDOT:PSS via consideration of the chemistry between MAI and isolated PSS ionomer. **a**, UV-Visible absorbance spectroscopy of isolated PSS ionomer solution with increasing concentrations of MAI leading to the presence of a new peak at 366 nm. **b**, Mass spectrum of PSS combined with equimolar MAI showing high concentrations of I_3^- and residual unreacted I_2. **c**, UV-Visible absorbance spectra comparing PSS + equimolar MAI with various reference spectra, confirming the new peak as I_3^-.

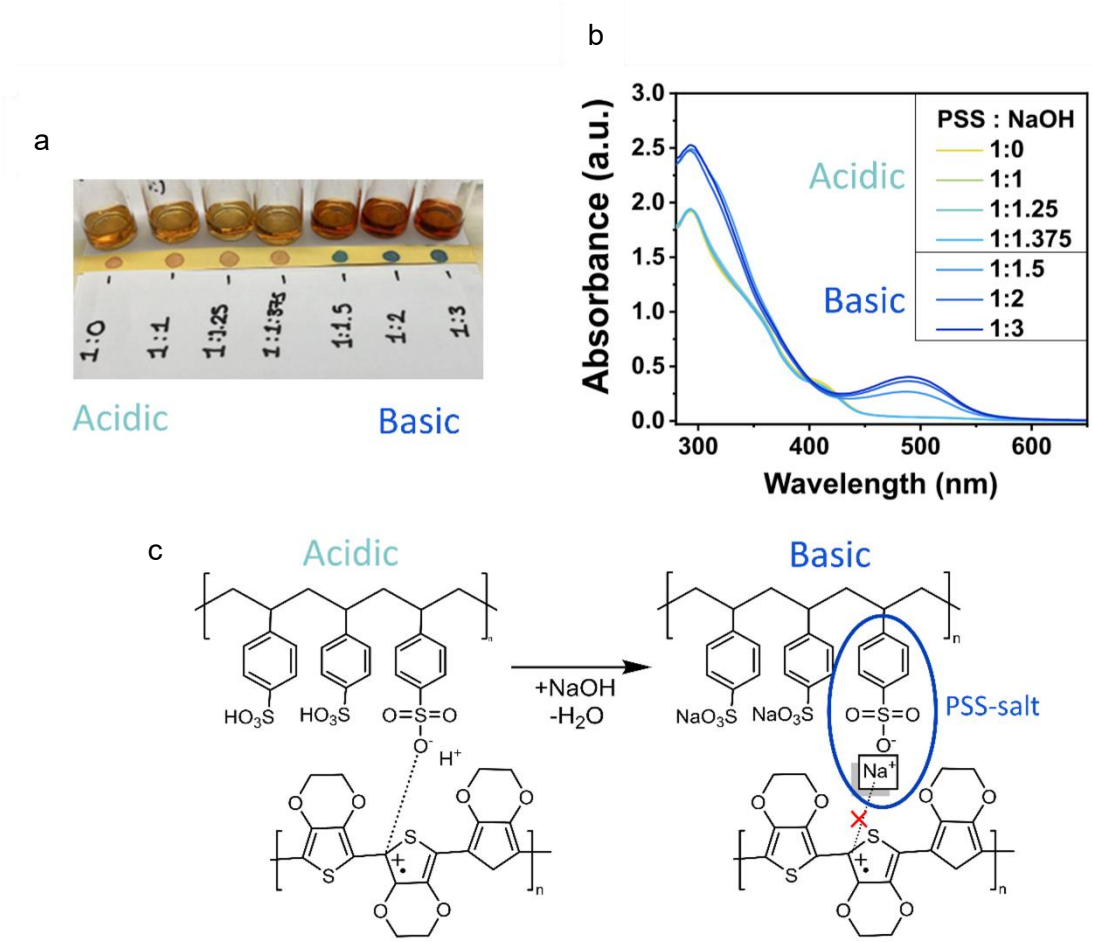

Supplementary Fig. 19. Mechanism of PSS de-doping from the combination with NaOH to understand the origin of aforementioned PEDOT:PSS de-doping with NaOH. **a**, Photograph of PSS solution with increasing NaOH concentrations turning pH indicating paper from red (acidic) to blue (alkaline) with a transition at a molar ratio of 1:1.375 PSS to NaOH, consistent with an acid-base neutralisation and the formation of a salt. **b**, UV-visible absorbance spectra of PSS ionomer combined with increasing molar ratios of NaOH. A distinct change in the absorbance profile is noted upon neutralisation of the acid accompanied by a new peak at approximately 490 nm as well as enhancement of the peak at 300 nm. **c**, Mechanism of acid (PSS) and base (neutralisation) leading to the formation of a $PSS^{-}Na^{+}$ salt and destabilising of positive charges on the PEDOT chain.

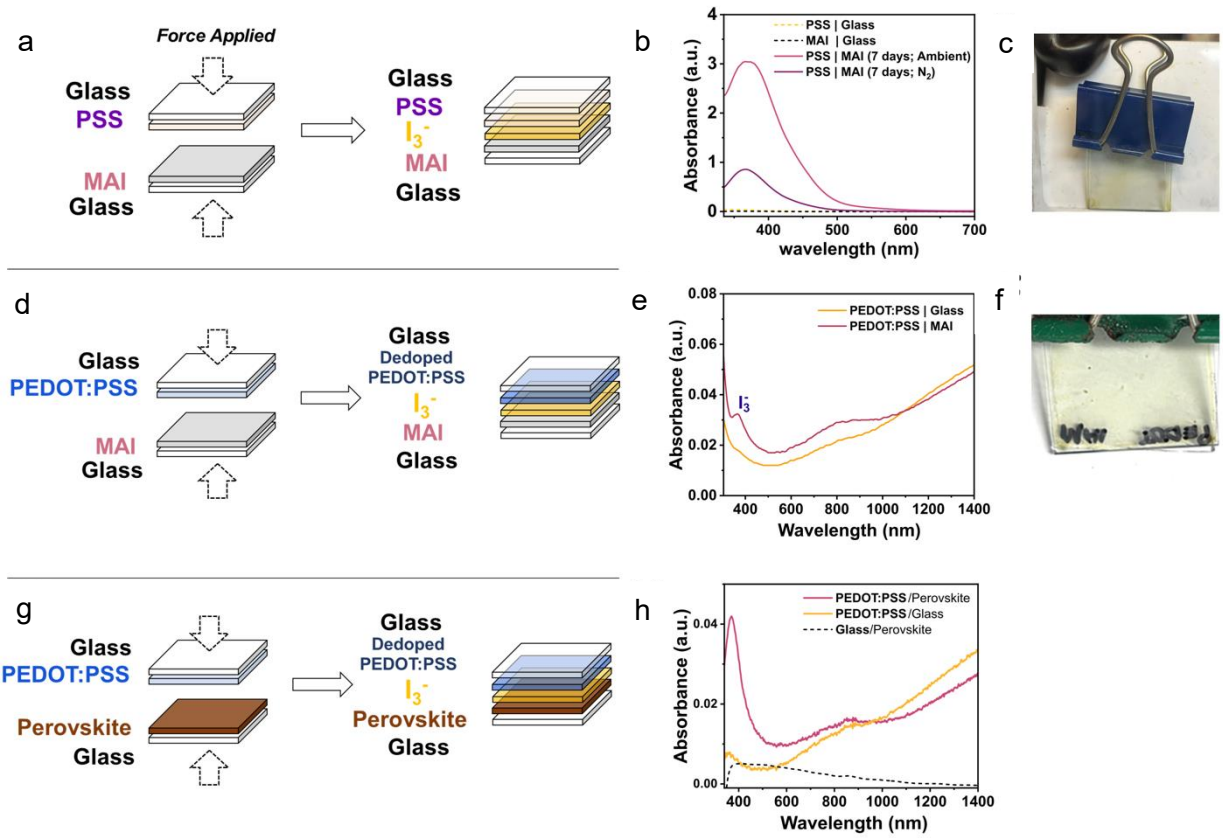

Supplementary Fig. 20. Experiments to investigate the chemistry between PEDOT:PSS and MAPI at a solid-state interface. **a-c**, Investigation into the reaction between PSS and MAI in the solid-state, **a**, schematic of experiment design where glass substrates coated in PSS and glass substrates coated in MAI were pressed together. **b**, Absorbance spectra of PSS substrate after 7 days in either ambient or N_2 conditions showing a large peak centred at 366 nm. **c**, Photograph of PSS coated glass following pressing against MAI within a nitrogen filled glovebox (<0.5 ppm O_2) for 1 week. **d-f**, Investigation into the reaction between PEDOT:PSS and MAI **d**, Schematic where PEDOT:PSS coated glass substrates are pressed against glass with and without an MAI layer for 48 h. **e**, Absorbance spectra of PEDOT:PSS films following pressing against MAI or glass (control). **f**, Photograph of PEDOT:PSS following pressing against MAI for 48 h in ambient conditions, where the yellow hue is attributed to the formation of I_3^-. **g-h**, Investigating into the reaction between PEDOT:PSS and MAPI, which represents a full PEDOT:PSS/perovskite heterojunction. **g**, Schematic of experimental design where PEDOT:PSS coated glass substrates are pressed against either glass (control) or MAPI films. **h**, Absorbance spectra of PEDOT:PSS films following pressing against glass (control) or MAPI.

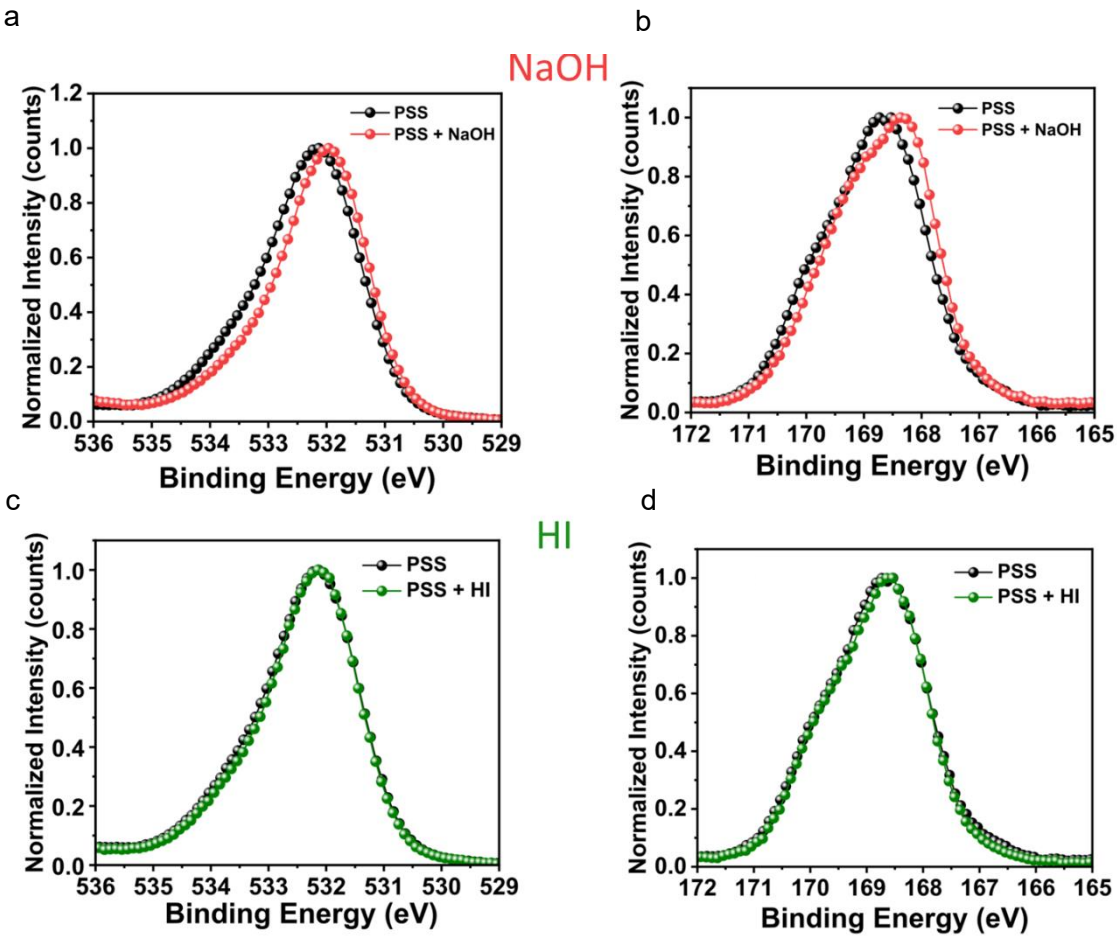

Supplementary Fig. 21 X-ray photoelectron spectroscopy measurements on the reaction between NaOH (Arrhenius Base) and HI on PSS. **a-b,** XPS spectra of the reaction between PSS and NaOH of the **a**, O 1s orbital and **b**, S 2p orbitals revealing changes to the sulfonate group of PSS upon the addition of NaOH. **c-d**, XPS spectra of the reaction between PSS and HI of the **c**, O 1s orbital and **d**, S 2p orbitals revealing no significant changes to the sulfonate group of PSS upon the addition of HI. In **b**, the peak splitting for S2p signal resulting from the spin orbit coupling is less prominent for PSS:Na compared to that for PSS:organic cation, due to the weaker interaction between PSS and Na^+ compared to the latter.

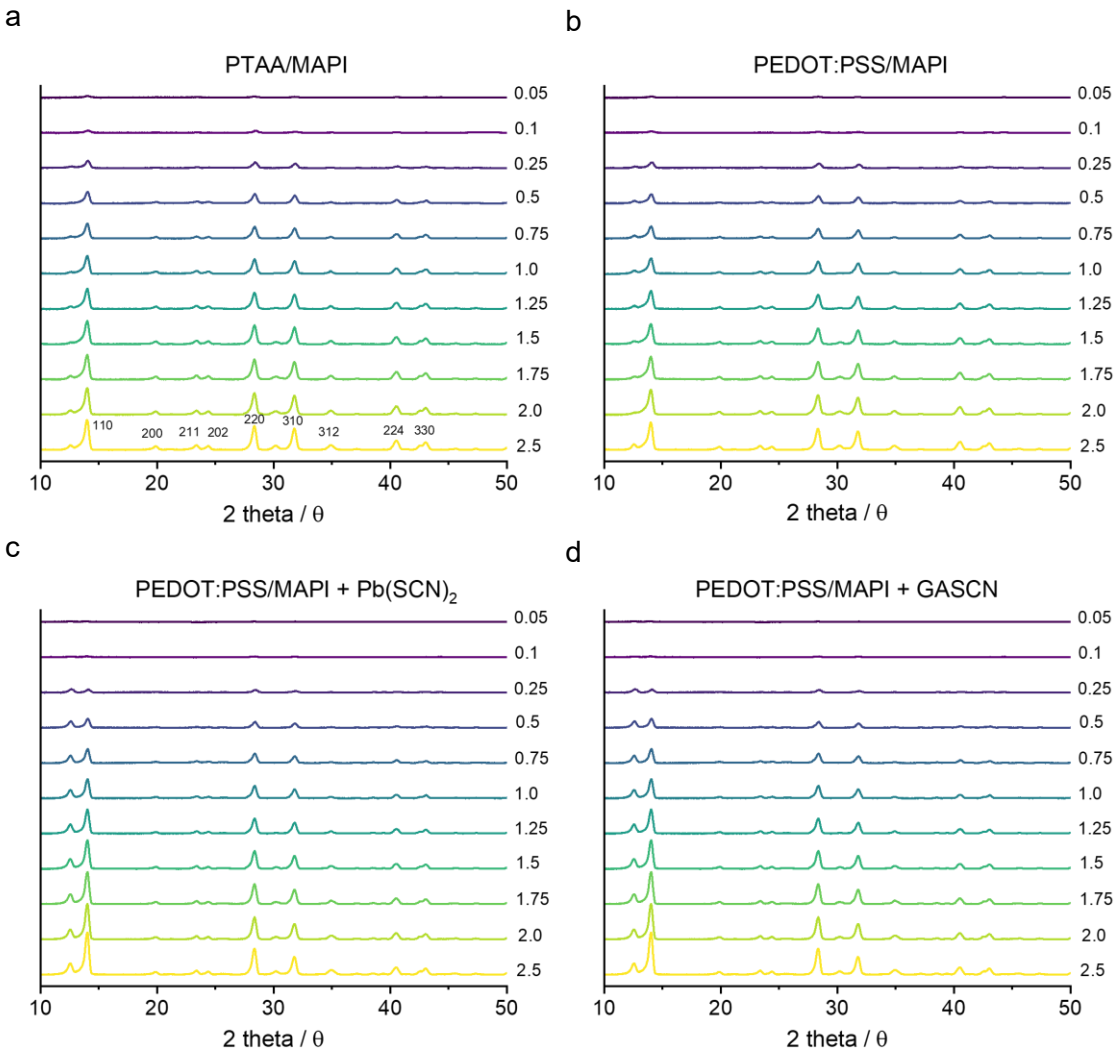

Supplementary Fig. 22. GIXRD spectra of perovskite films at grazing angles ranging from 0.05° to 2.5°. **a**, PTAA/MAPI, **b**, PEDOT:PSS/MAPI, **c**, PEDOT:PSS/MAPI + $Pb(SCN)_2$, and **d**, PEDOT:PSS/MAPI + GASCN.

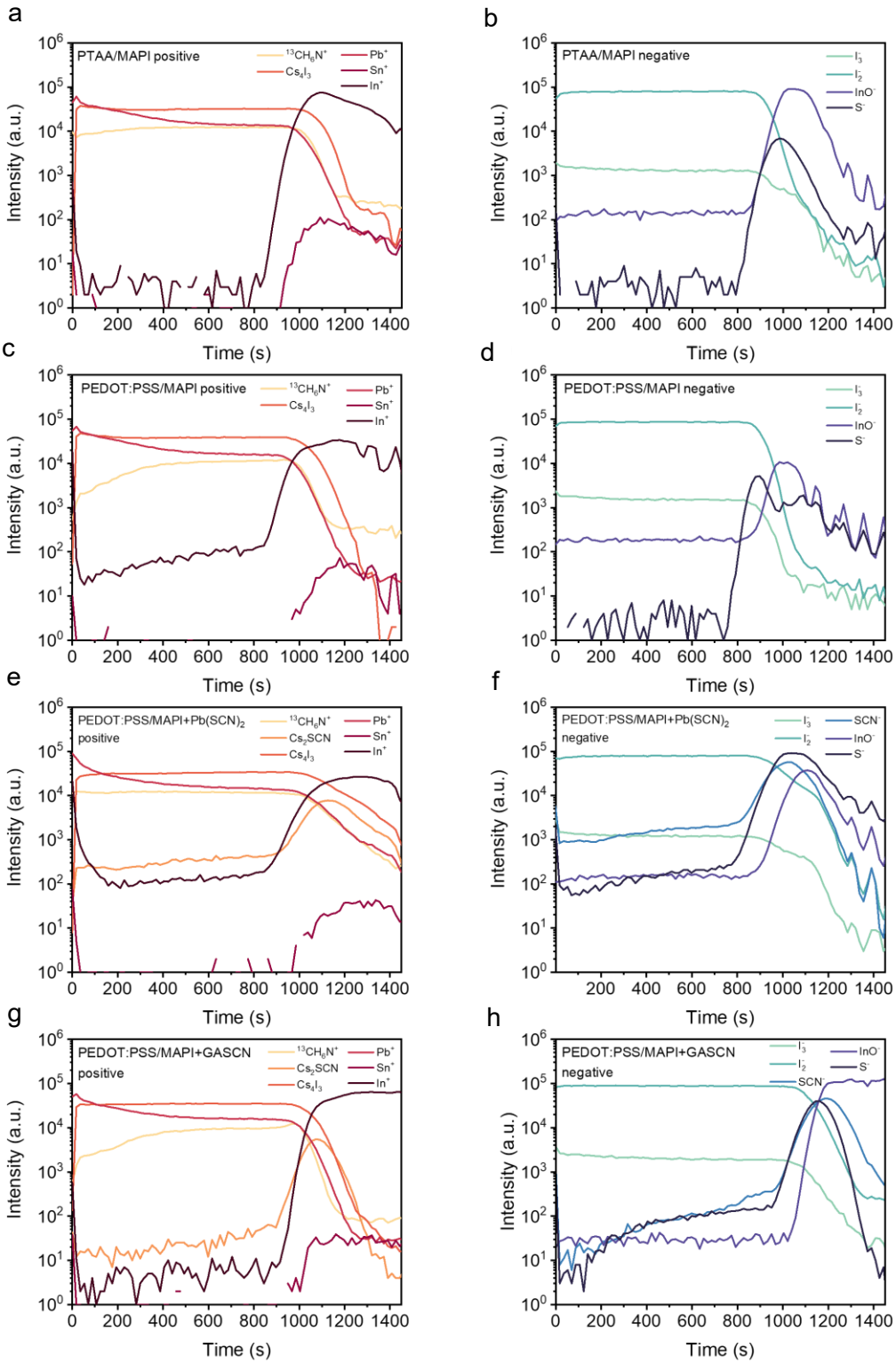

Supplementary Fig. 23. ToF-SIMS of half cells. Positive and negative ToF-SIMS depth profiles for, **a**, and **b**, PTAA/MAPI, **c**, and **d**, PEDOT:PSS/MAPI, **e** and **f**, PEDOT:PSS/MAPI + $Pb(SCN)_2$, and **g** and **h**, PEDOT:PSS/MAPI + GASCN.

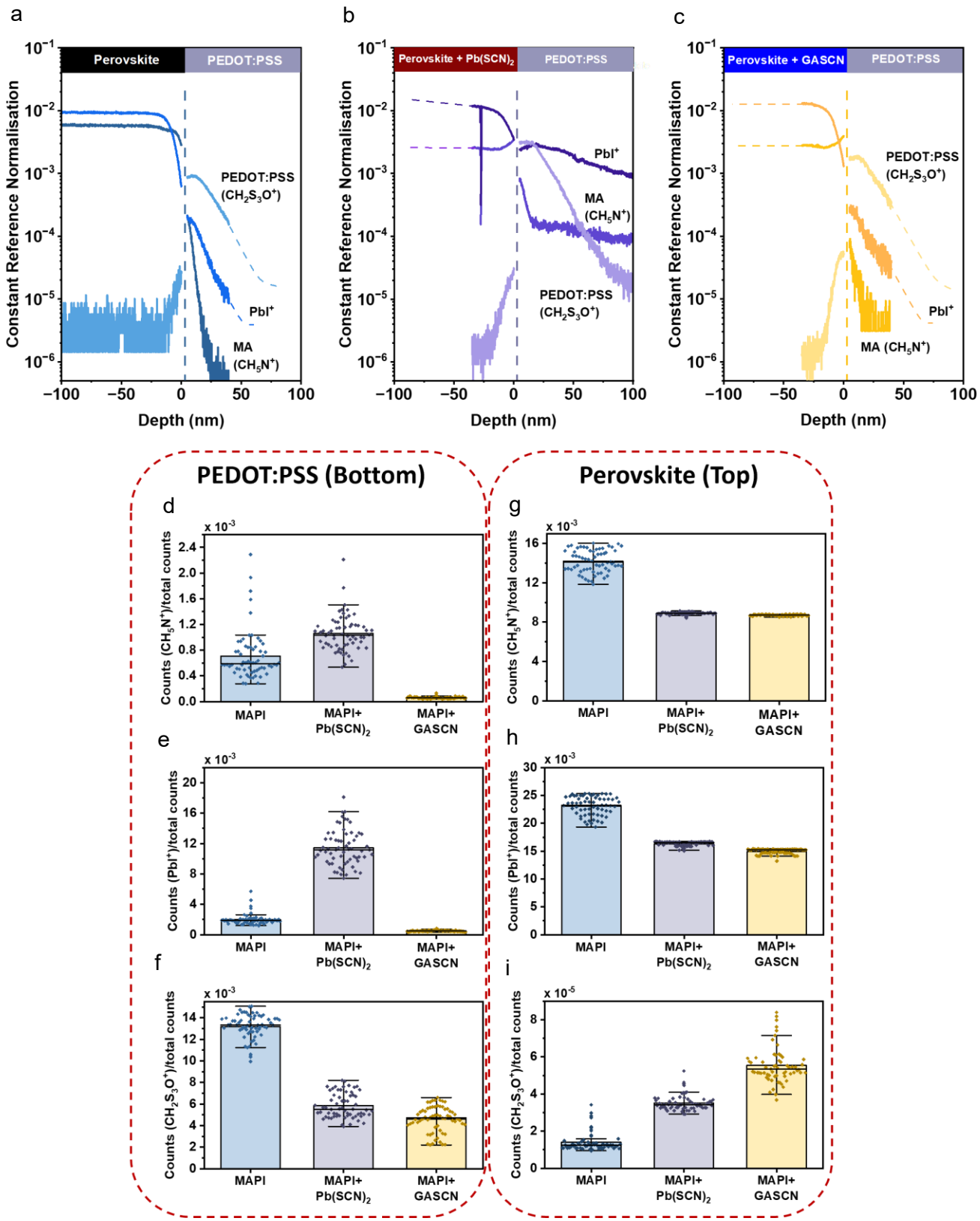

Supplementary Fig. 24. Penetration of amines into PEDOT:PSS. ToF-SIMS depth profiles of **a**, PEDOT:PSS/MAPI, **b**, PEDOT:PSS/MAPI + $Pb(SCN)_2$ and **c**, PEDOT:PSS/MAPI + GASCN. Total intensity analysis of **d** – **f**, PEDOT:PSS (bottom) and **g** – **i**, perovskite absorber (top), indicating the distribution of MA, Pb and PSS content within each half of the sample. The spike observed in **b** between -50 and 0 nm is an experimental artefact.

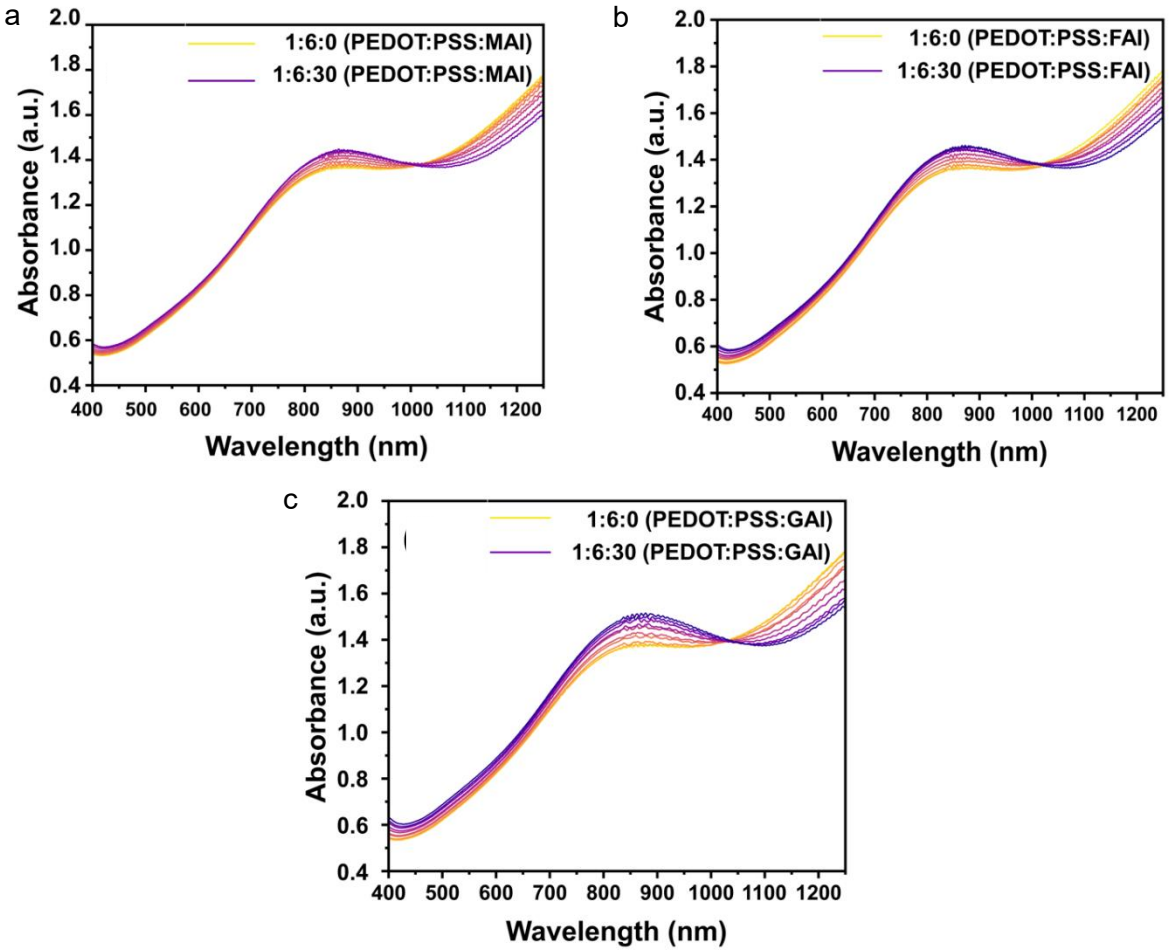

Supplementary Fig. 25. UV-visible absorbance spectra of PEDOT:PSS solution following the addition of increasing concentrations of common perovskite precursor salts **a**, Methylammonium iodide, **c**, Formamidinium iodide and **c**, guanidinium iodide. All samples were measured in a quartz cuvette of path length 1 mm.

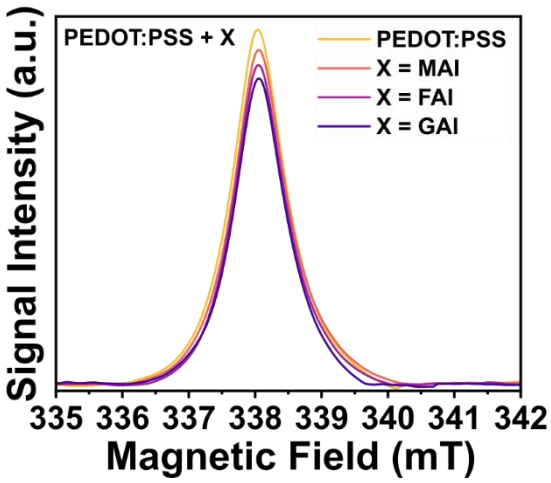

Supplementary Fig. 26. Integrated electron paramagnetic resonance spectra of PEDOT:PSS following the addition of common perovskite organohalide salts.

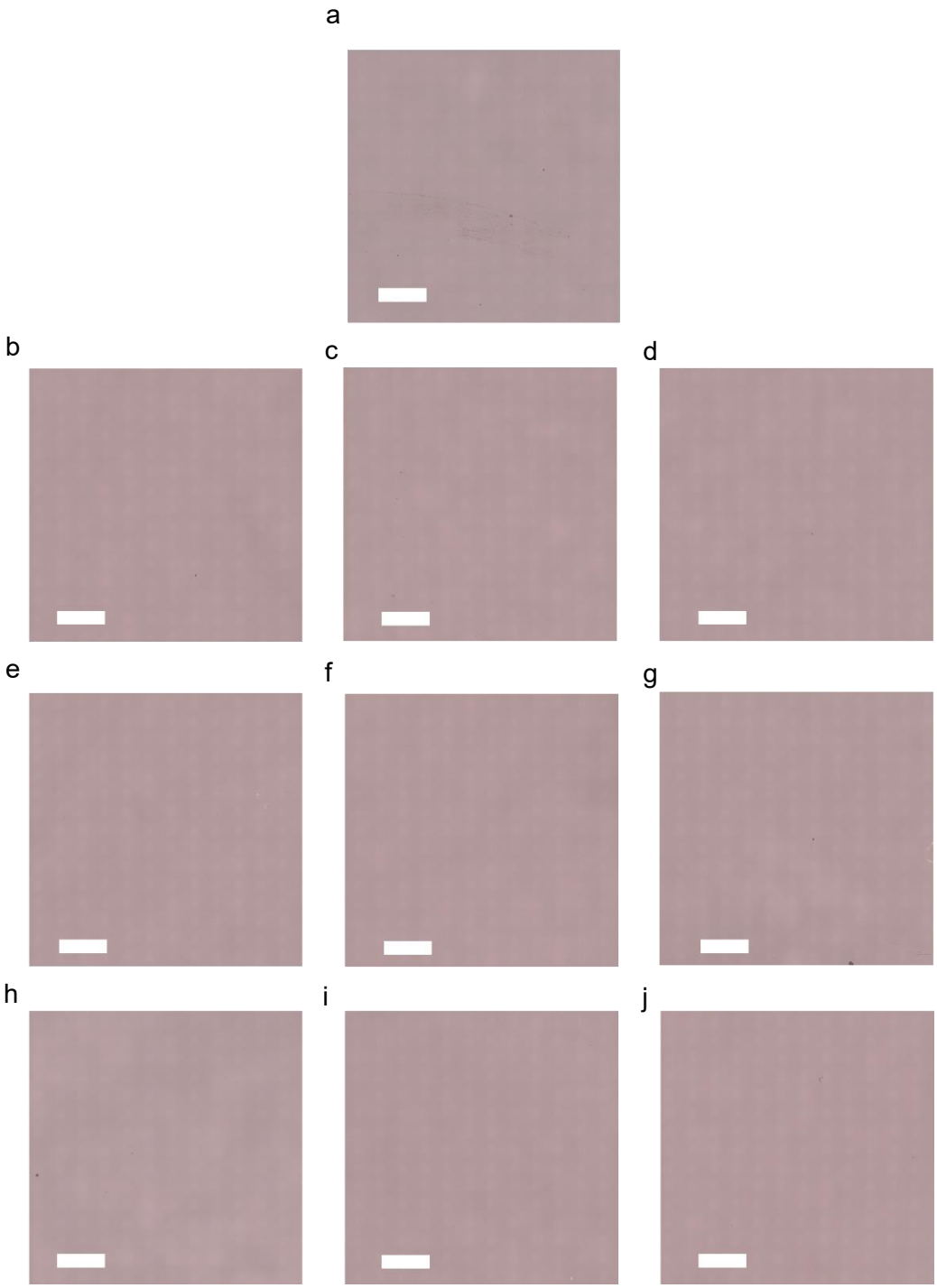

Supplementary Fig. 27. Optical micrographs of MAI added to PEDOT:PSS dispersions. The PSS:MA^+ molar ratios studied are, **a**, 1:0, **b**, 1:0.25, **c**, 1:0.50, **d**, 1:0.75, **e**, 1:1, **f**, 1:1.5, **g**, 1:2, **h**, 1:3, **i**, 1:4, and **j**, 1:5. The scale bar indicates 500 μm. The images do not indicate any visible aggregates within the blended films.

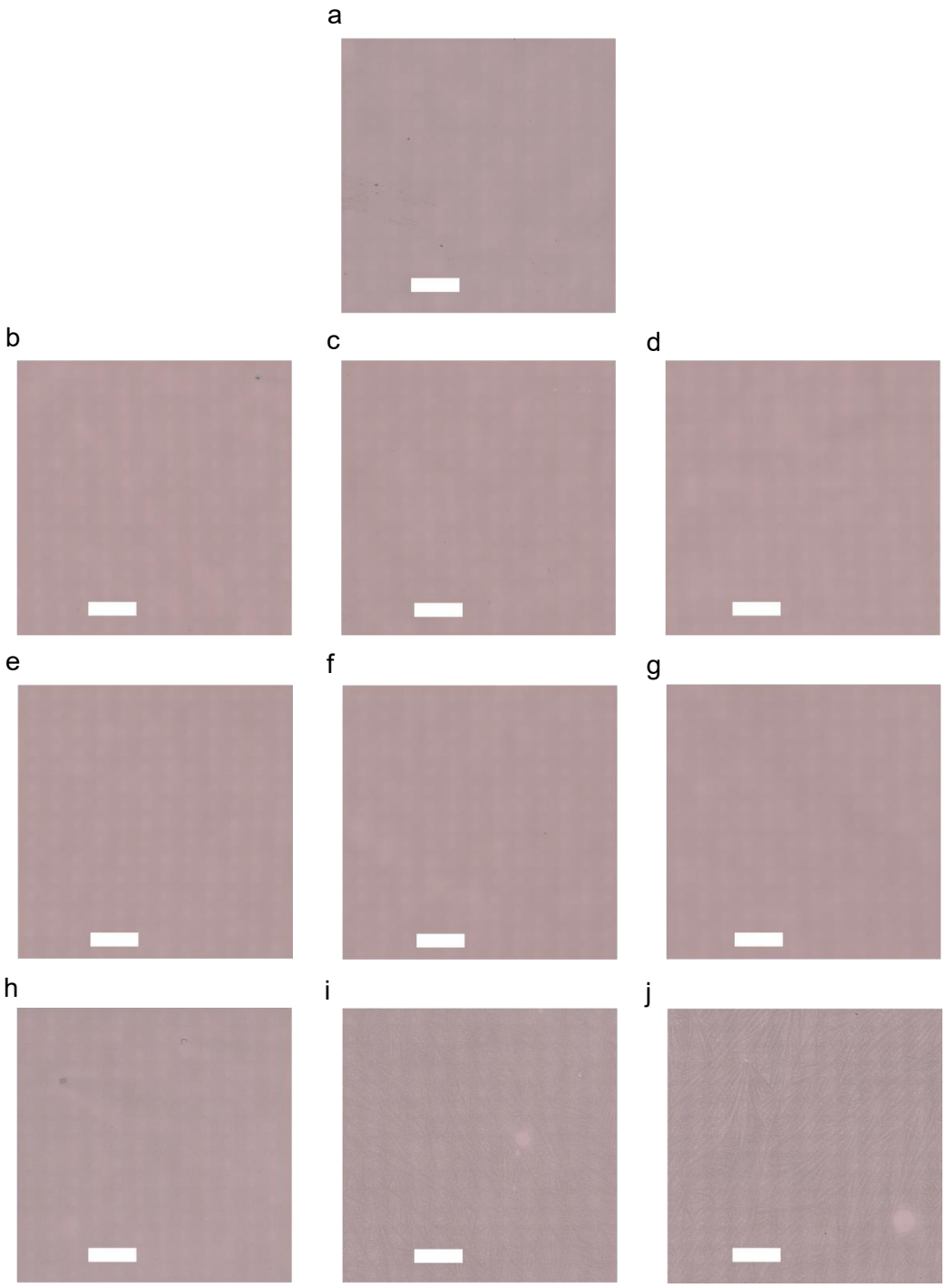

Supplementary Fig. 28. Optical micrographs of FAI added to PEDOT:PSS dispersions. The PSS:FA^+ molar ratios studied are, **a**, 1:0, **b**, 1:0.25, **c**, 1:0.50, **d**, 1:0.75, **e**, 1:1, **f**, 1:1.5, g, 1:2, **h**, 1:3, **i**, 1:4, and **j**, 1:5. The scale bar indicates 500 µm. Dendritic structures are visible at 1:4 and 1:5 ratios.

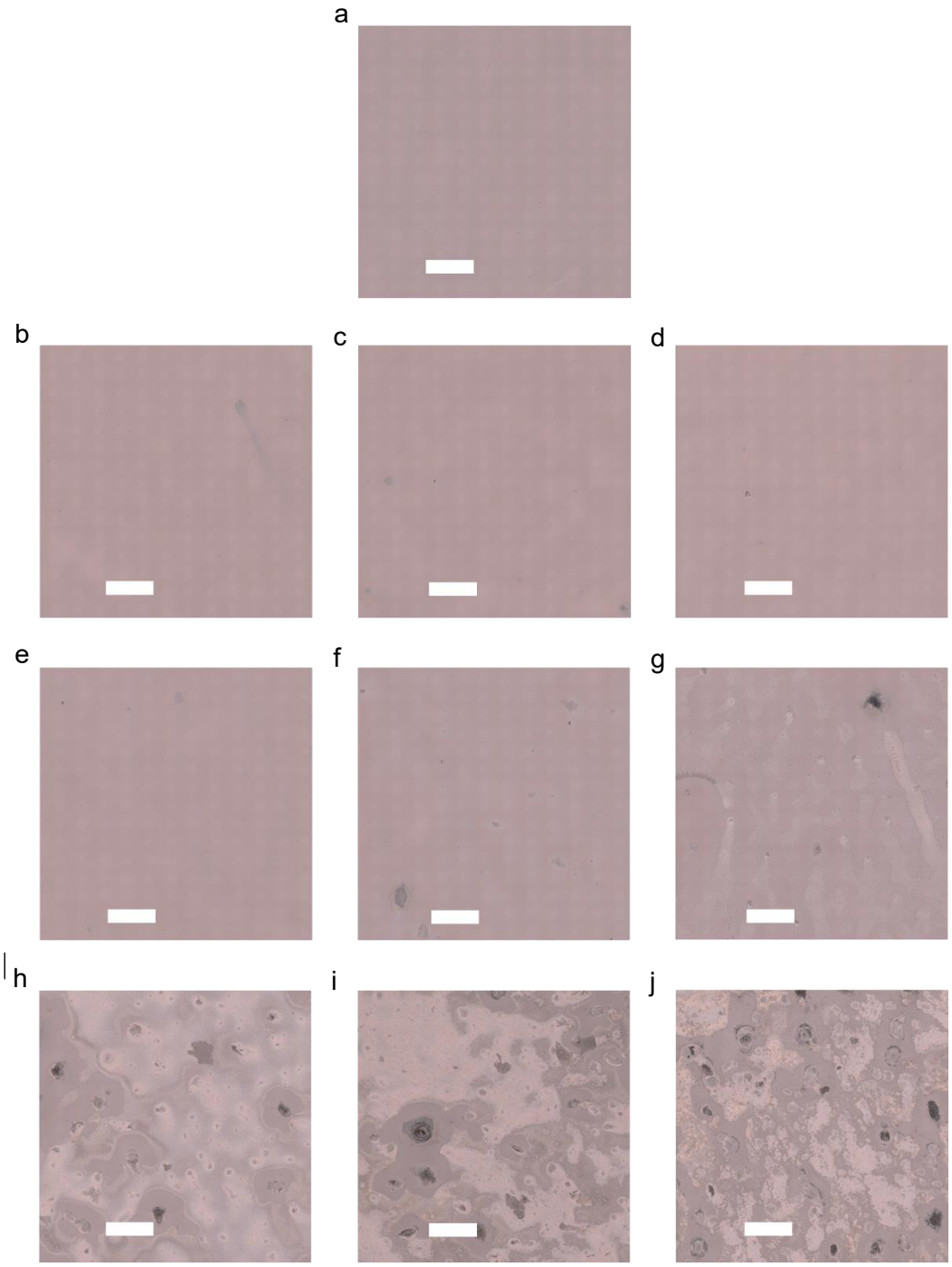

Supplementary Fig. 29. Optical micrographs of GAI added to PEDOT:PSS dispersions. The PSS:GA^+ molar ratios studied are, **a**, 1:0, **b**, 1:0.25, **c**, 1:0.50, **d**, 1:0.75, **e**, 1:1, **f**, 1:1.5, **g**, 1:2, **h**, 1:3, **i**, 1:4, and **j**, 1:5. The scale bar indicates 500 μm. The images indicate the emergence of aggregates from PSS:GA^+ ratios of 1:2 onwards which are formed following the deactivation of PSS with the organic cation.

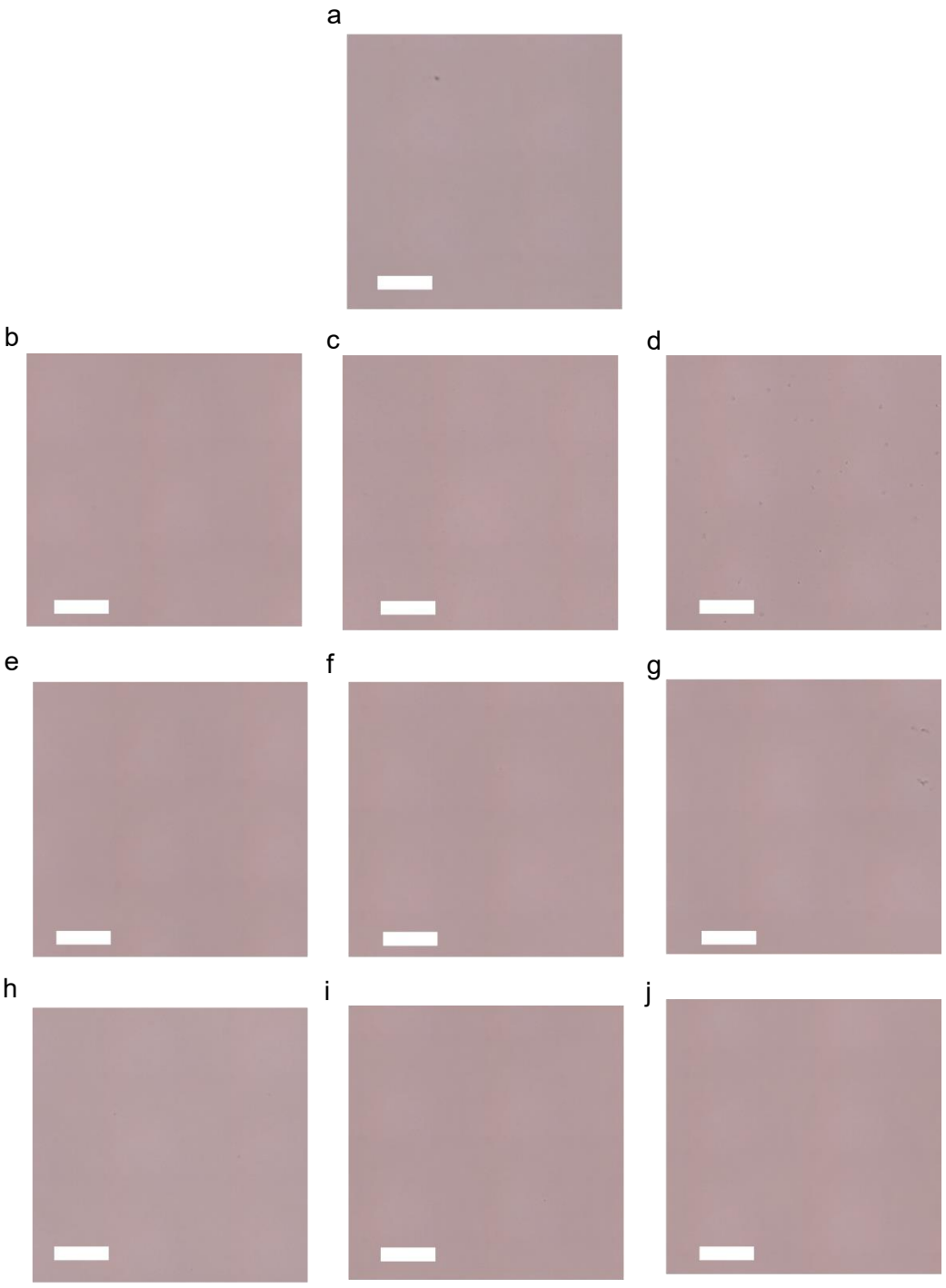

Supplementary Fig. 30. Higher magnification optical micrographs of MAI added to PEDOT:PSS dispersions. The PSS:MA^+ molar ratios studied are, **a**, 1:0, **b**, 1:0.25, **c**, 1:0.50, **d**, 1:0.75, **e**, 1:1, **f**, 1:1.5, **g**, 1:2, **h**, 1:3, **i**, 1:4, and **j**, 1:5. The scale bar indicates 100 μm. The images do not indicate any visible aggregates within the blended films.

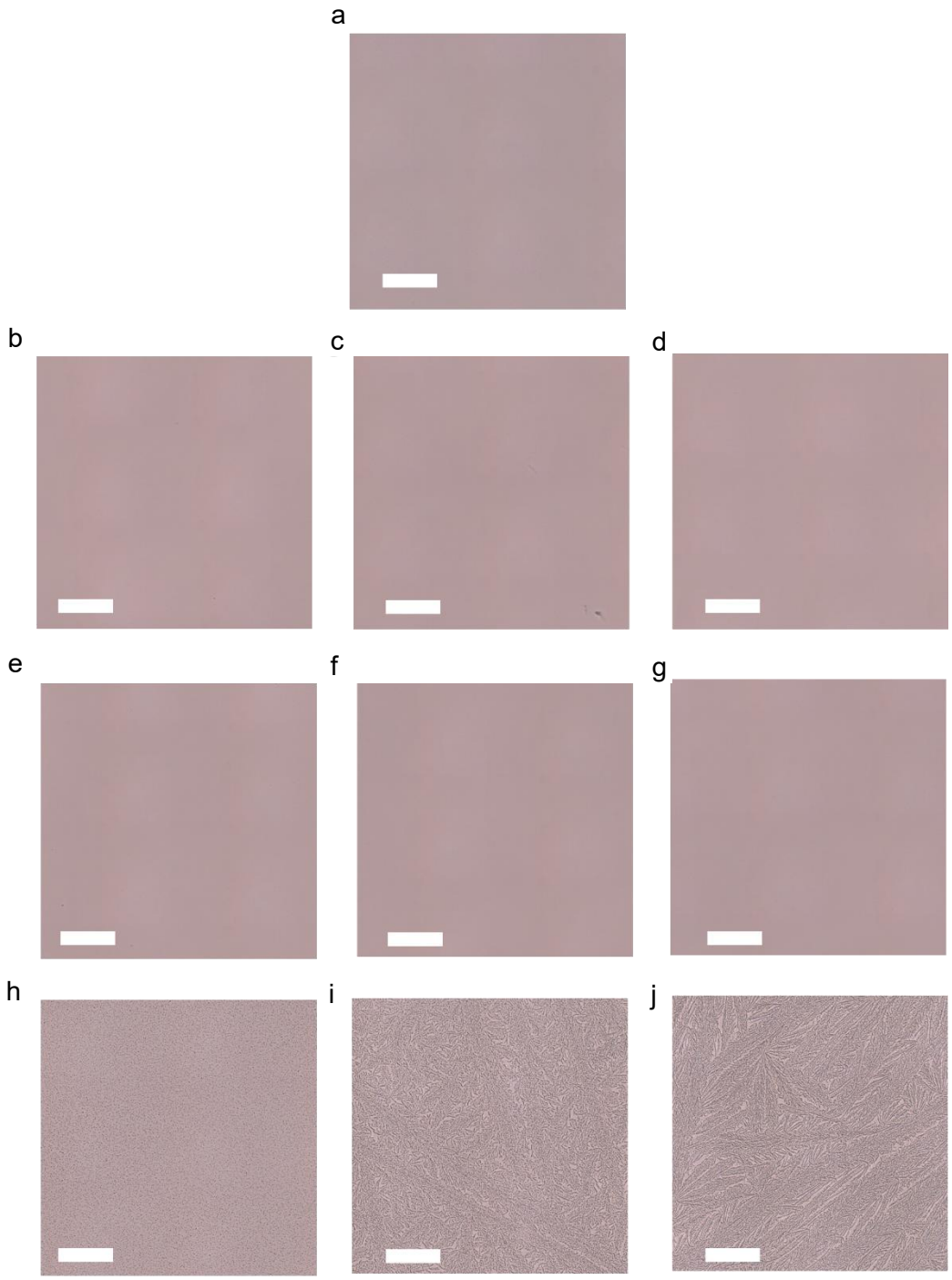

Supplementary Fig. 31. Higher magnification optical micrographs of FAI added to PEDOT:PSS dispersions. The PSS:FA^+ molar ratios studied are, **a**, 1:0, **b**, 1:0.25, **c**, 1:0.50, **d**, 1:0.75, **e**, 1:1, **f**, 1:1.5, **g**, 1:2, **h**, 1:3, **i**, 1:4, and **j**, 1:5. The scale bar indicates 100 µm. The images indicate the emergence of fine aggregates from PSS: FA^+ ratios of 1:3 onwards which are formed following the deactivation of PSS with the organic cation with dendritic structures being evident at 1:4 and 1:5.

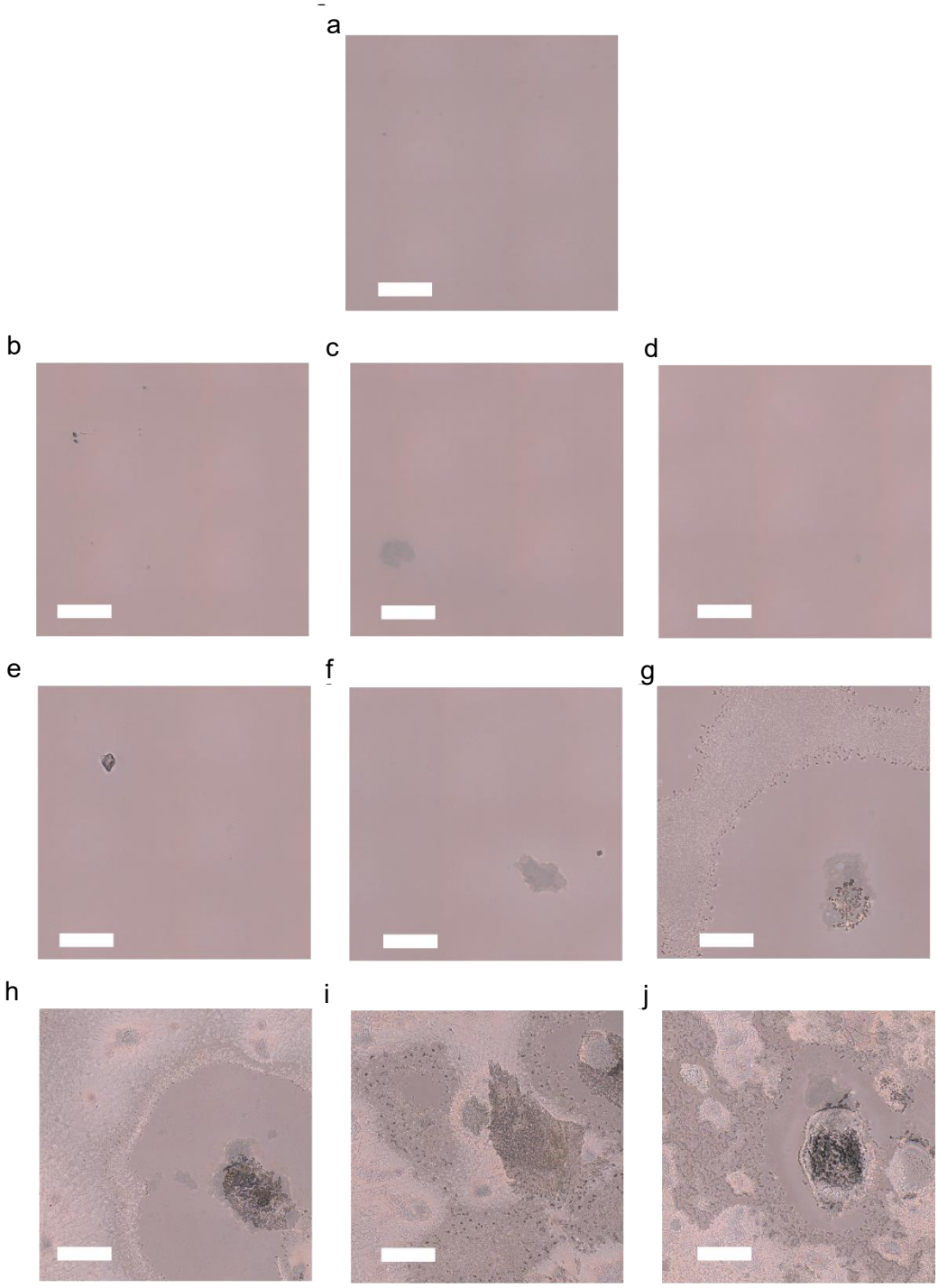

Supplementary Fig. 32. Higher magnification optical micrographs of GAI added to PEDOT:PSS dispersions. The PSS:GA^+ molar ratios studied are, **a**, 1:0, **b**, 1:0.25, **c**, 1:0.50, **d**, 1:0.75, **e**, 1:1, **f**, 1:1.5, **g**, 1:2, **h**, 1:3, **i**, 1:4, and **j**, 1:5. The scale bar indicates 500 µm. The images indicate the emergence of aggregates from PSS:GA^+ ratios of 1:1.5 onwards which are formed following the deactivation of PSS with the organic cation.

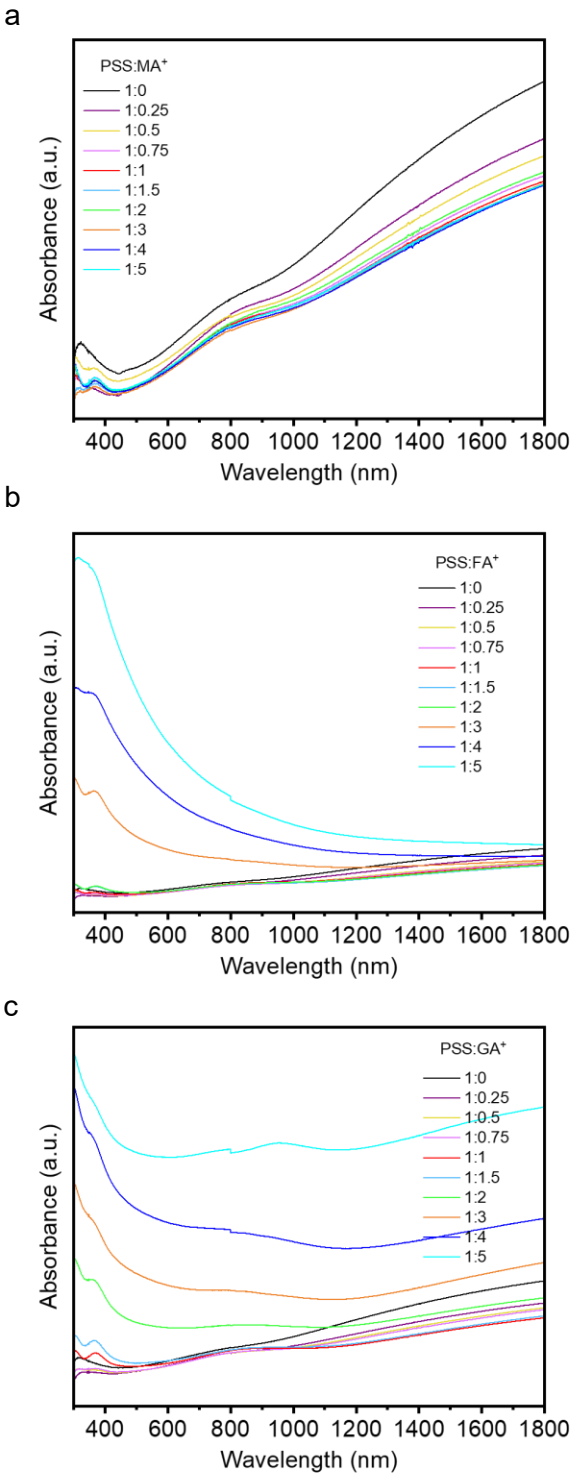

Supplementary Fig. 33. UV-Visible spectra of organohalides added to PEDOT:PSS. **a**, MAI, **b**, FAI, and **c**, GAI at PSS:organic cation ratios of 1:0, 1:0.25, 1:0.50. 1:0.75, 1:1, 1:1.5, 1:2, 1:3, 1:4 and 1:5.

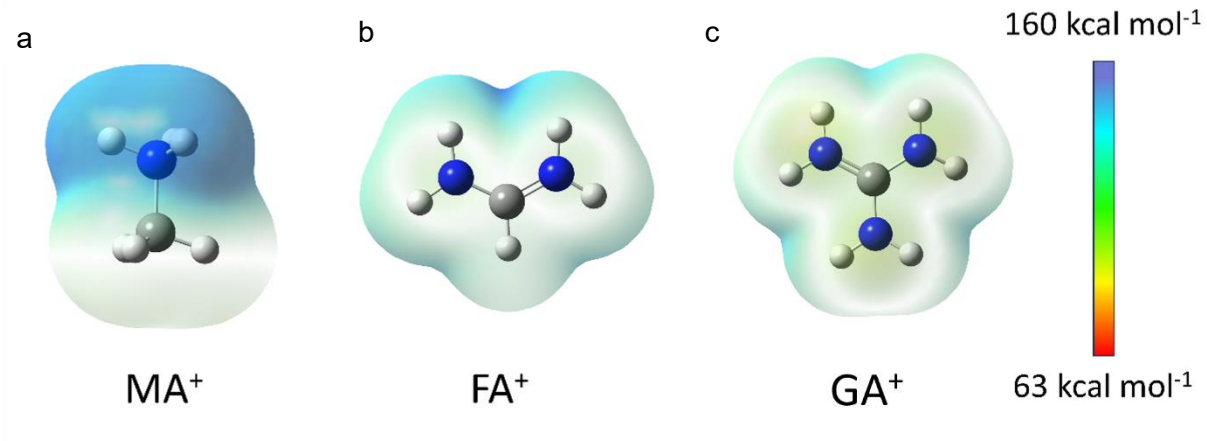

Supplementary Fig. 34. Electronic potential surfaces of organic cations showing the effect of delocalisation on positive charge distribution on **a**, MA^+, **b**, FA^+ and **c**, GA^+.

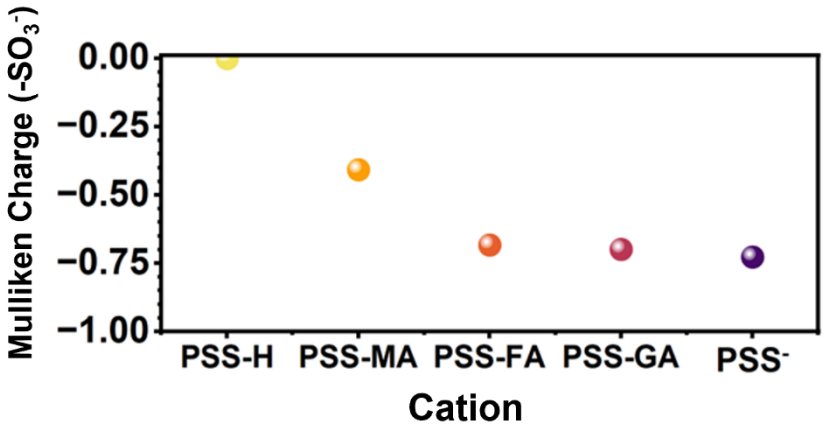

Supplementary Fig. 35. Integrated predicted Mulliken charge across the sulfonate $(-SO_3^-)$group of PSS with various organic cations.

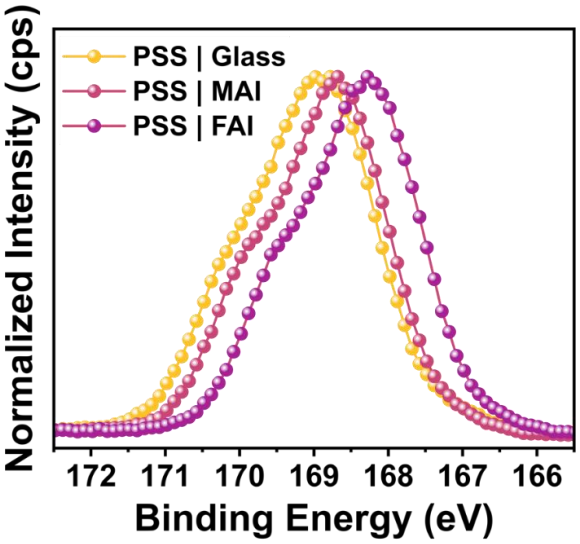

Supplementary Fig. 36 X-ray photoelectron spectroscopy of PSS sulfonate S 2p orbital following pressing against glass (control), MAI and FAI. XPS data shows a greater shift in the S 2p indicating greater electron density in the sulfonate group following the creation of an interface with MAI and FAI. As predicted by DFT the greater delocalisation in the FA^+ cation leads to a larger shift in the S 2p and therefore greater electron density on the sulfonate group.

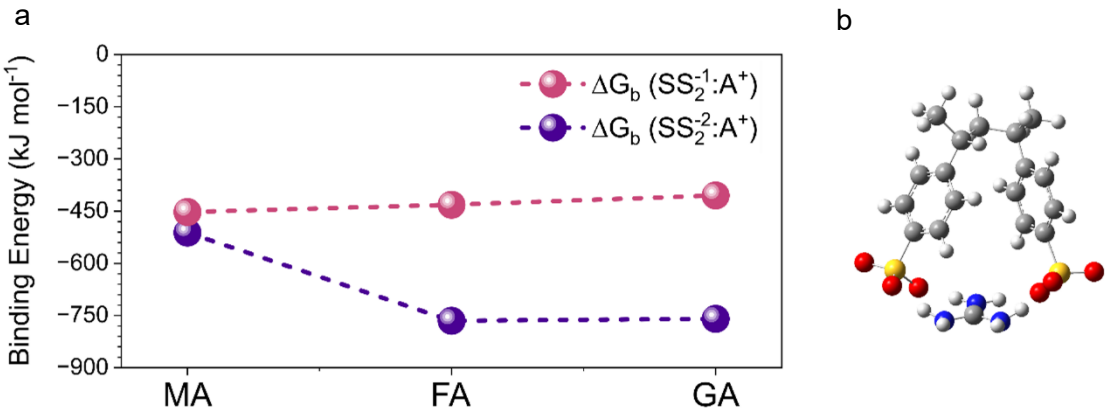

Supplementary Fig. 37. Comparison of 1PSS monomer (SS_1^{-1}) and 2 neighbouring PSS monomers (SS_2^{-2}). **a**, Comparison of the predicted binding energies. **b**, Optimised molecular geometry of SS_2^{-2}:GA^+ showing the delocalisation of charge across the molecule enables bridging between 2 neighbouring PSS monomers.

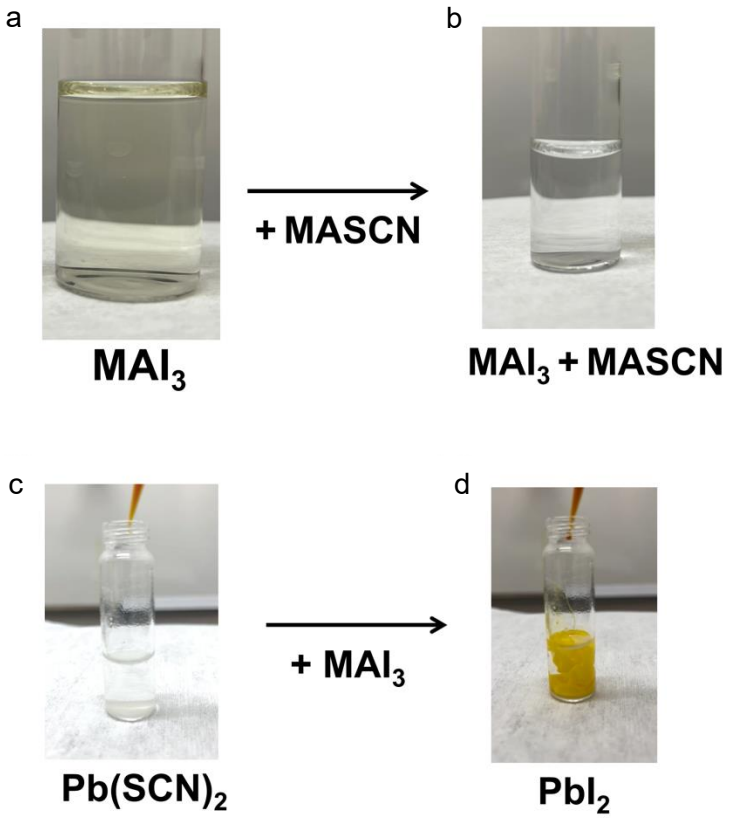

Supplementary Fig. 38. Reaction between MAI_3 with various ^-SCN salts. **a**-**d**, Photographs of **a**, MAI_3 solution prepared by the combination of MAI with I_2 and **b**, following addition of MASCN thiocyanate additive leading to a colour change to colourless indicative of the reduction of I_2 to I^-. **c**, Photograph of $Pb(SCN)_2$ solution and pipette containing MAI_3 solution, **d**, photograph of the same solution following the addition of MAI_3 forming a bright yellow distinctive PbI_2 precipitate.

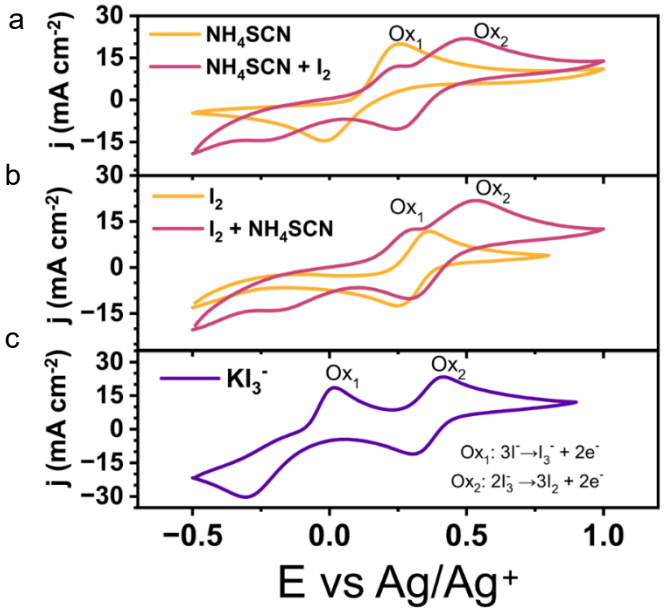

Supplementary Fig. 39 Cyclic Voltammetry using an anhydrous 0.15 M nBu_4PF_6 acetonitrile electrolyte solvent, degassed under N_2, combined with $AgNO_3$ electrode**. a**, Voltammogram of NH_4SCN before (yellow) and after (pink) the addition of I_2. **b**, Voltammogram of I_2 ACN solution before (yellow) and after (pink) the addition of NH_4SCN. **c**, Reference KI_3 solution showing the two distinct oxidation/reduction peaks associated with I_3^- equilibria ($[I^-]$:$[I_3^-]$:$[I_2]$).

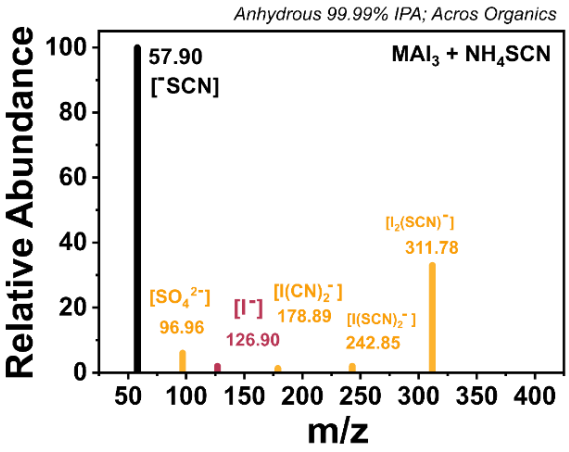

Supplementary Fig. 40. Mass Spectrometric analysis with electrospray ionisation of MAI_3 in isopropyl alcohol (IPA) after the addition of NH_4SCN, showing the intermediates of the reaction between SCN^- and I_3^-.

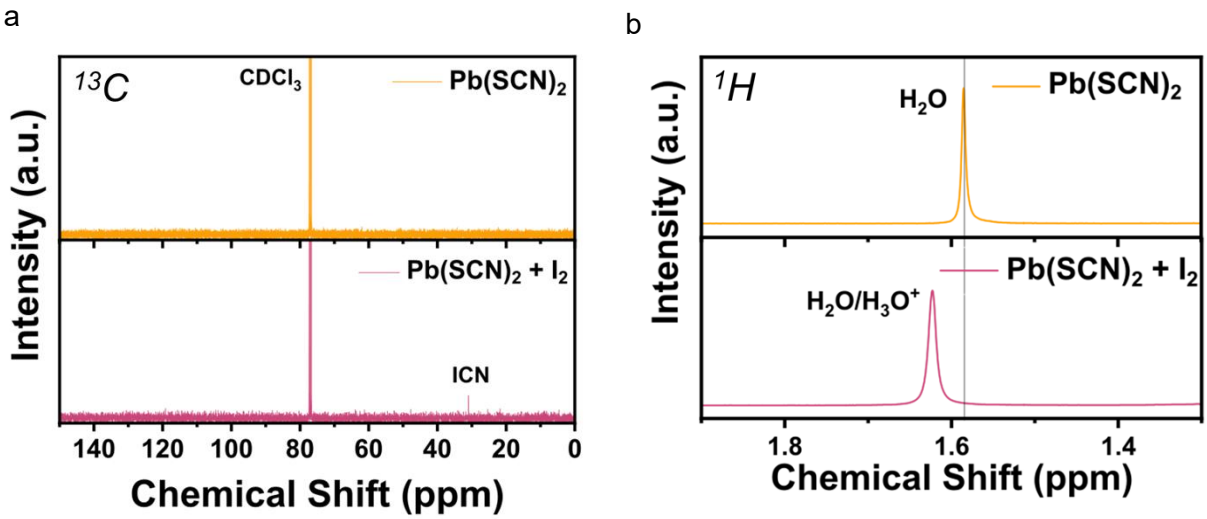

Supplementary Fig. 41. NMR spectra investigating the formation of iodine thiocyanogen via the combination of $Pb(SCN)_2$ and I_2, **a**, ^{13}C NMR spectra of (top) $Pb(SCN)_2$ dispersed in $CDCl_3$ and (bottom) the same $Pb(SCN)_2$ suspension following addition of I_2 revealing the transformation of the SCN^- ion. We note the peak at 33 ppm is too shielded to be attributed to the SCN^- ion (~133 ppm). **b**, ^1H NMR spectra of the solutions measured in **b** showing de-shielding of the H_2O trace water peak indicative of the formation of H_3O^+ and acidification of the solution, in this case, H_2SO_4.

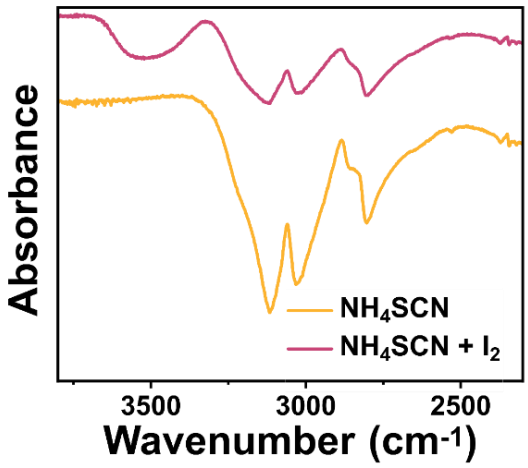

Supplementary Fig. 42. FTIR spectra of NH_4SCN crystals following exposure to I_2 vapor in ambient conditions leading to the formation of a new peak at 3600 cm^{-1}, attributed to H_2SO_4.

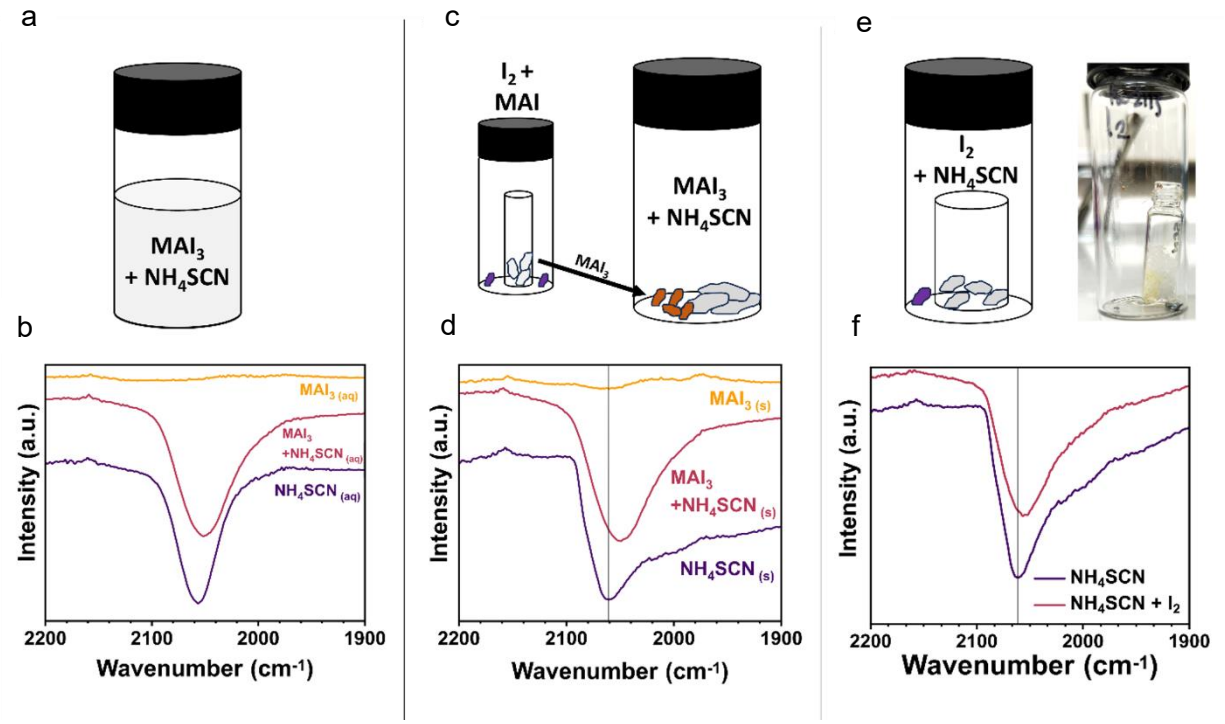

Supplementary Fig. 43. Attenuated Total Reflectance Fourier Transform Infrared Spectroscopy (ATR-FTIR) characterisation of the reaction between iodine and thiocyanates. **a**, Schematic of the liquid phase reaction between MAI_3 and NH_4SCN and **b**, IR spectrum, where the peak at 2050 cm^{-1} corresponds to the C-N triple bond. **c**, Schematic of the solid-solid interaction of NH_4SCN with MAI_3, prepared via exposing MAI powder to I_2 vapour and **d**, associated IR spectra showing an identical shift of the C-N bond to lower vibrational frequencies. **e**, Schematic of reaction between solid NH_4SCN powder and I_2 vapor, where solid-solid contact between the iodine pellet and NH_4SCN powder was avoided and **f**, resulting IR spectrum showing an identical shift to lower vibrational frequencies of the C-N bond following I_2 vapor exposure.

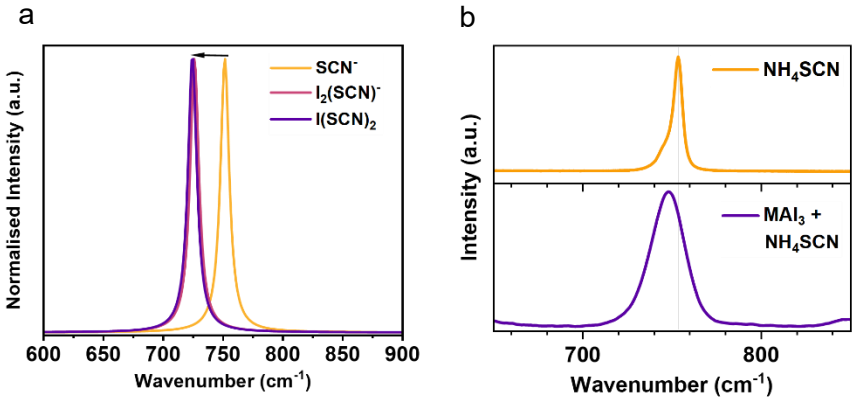

Supplementary Fig. 44. Confocal Raman vibrational spectroscopy of NH_4SCN reaction with MAI_3 in the solid-state. **a**, DFT prediction of the C-S shift in SCN^- anion and intermediate compounds identified within the mass spectrum. **b**, Experimental Raman of NH_4SCN powder and NH_4SCN powder following reaction with MAI_3 within the solid-state, showing a decrease in the frequency of the C-S vibrational mode.

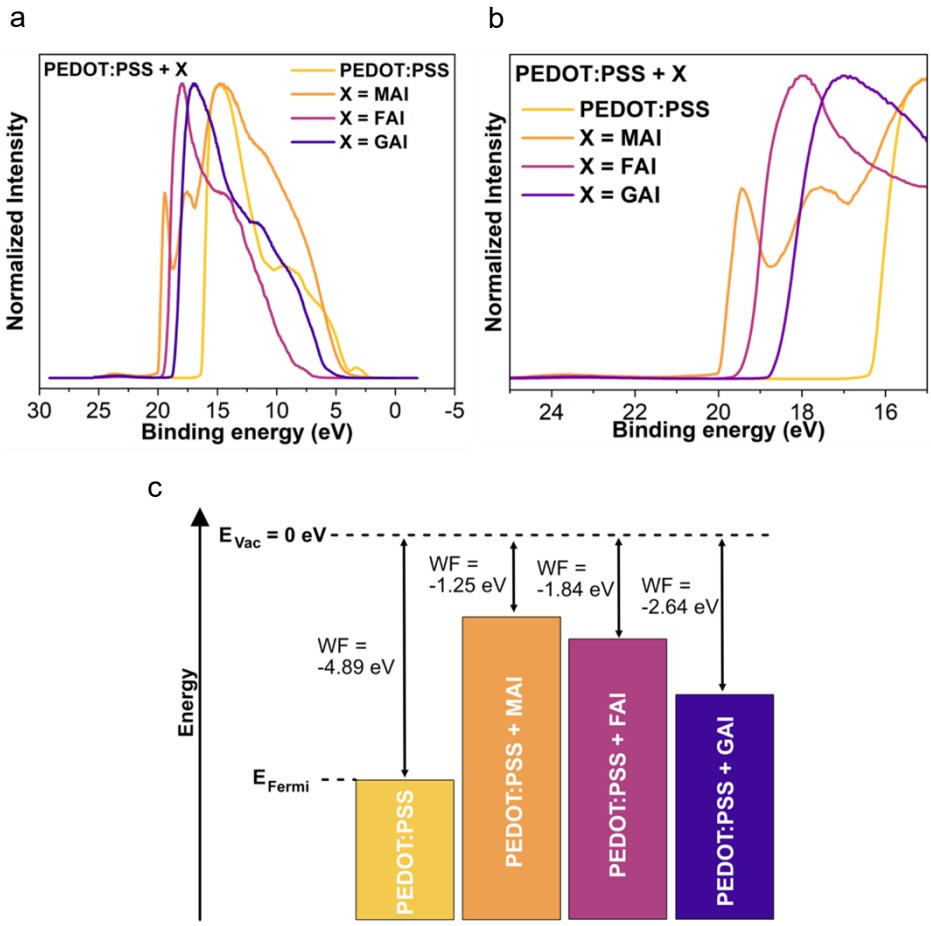

Supplementary Fig. 45. Changes in PEDOT:PSS work function following contact with different organohalides. **a** and **b,** Valence band spectra of PEDOT:PSS (ref) and PEDOT:PSS films brought into contact with MAI, FAI and GAI films. **c**, Changes to the PEDOT:PSS work function following 48 h pressing against films of either glass (control), MAI, FAI or GAI. In this experiment the change in work function is presented to demonstrate the ability of all tested organic cations to influence the interfacial energetics which is well reported to strongly influence device performance. We note that in a real device architecture the diffusion of organic cations into the PEDOT:PSS will be smaller than presented here which is presented for demonstrative purposes.

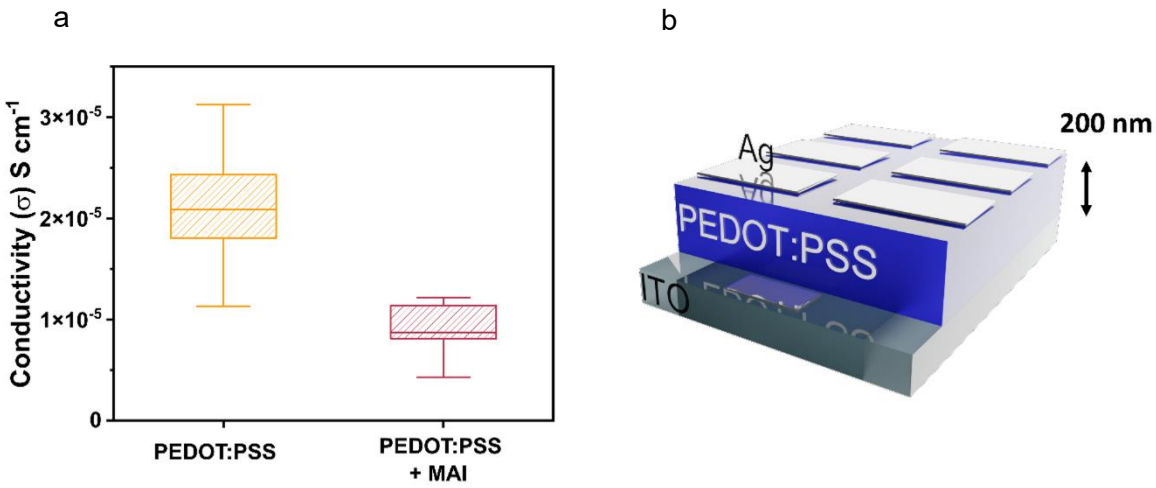

Supplementary Fig. 46. Measurement of PEDOT:PSS conductivity. **a**, Comparison of conductivity of PEDOT:PSS with and without equimolar MAI added directly to the solution pre-deposition. **b**, Schematic of architecture used to measure the conductivity of PEDOT:PSS across a 200 nm thin film of PEDOT:PSS.

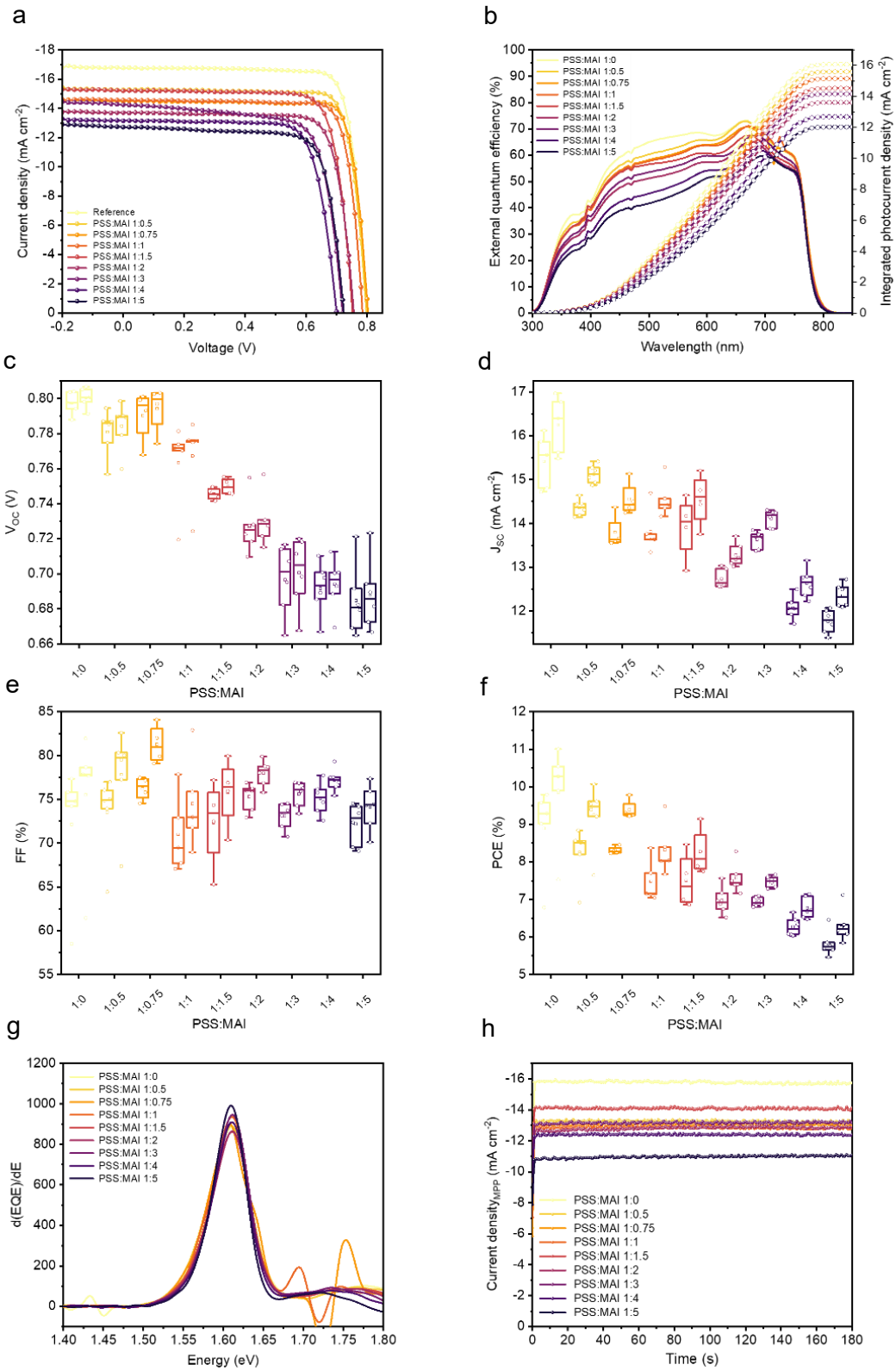

Supplementary Fig. 47. Performance characteristics of PEDOT:PSS/MAPI devices with additional MAI incorporated to PEDOT:PSS. **a**, *J-V* curves of champion devices (reverse scans). **b**, Corresponding EQE spectra and integrated J_{SC}. Box plots for **c**, V_{OC}, **d**, J_{SC}, **e**, FF, and **f**, PCE. **g**, Differential of EQE. **h**, Stability of the photocurrent at maximum power point as determined from *J-V* scans.

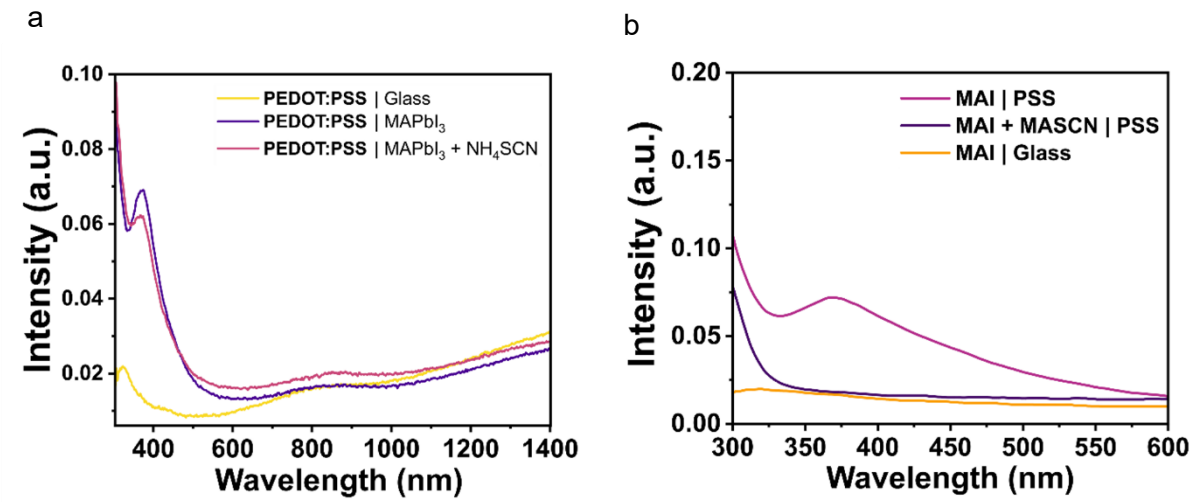

Supplementary Fig. 48. UV-Visible absorbance spectra characterising the effect of SCN^- salt incorporation within a perovskite active layer on the properties of PEDOT:PSS. **a**, Absorbance spectra of PEDOT:PSS films pressed against MAPI with and without NH_4SCN after aging in ambient conditions for 24 h. **b**, Effect of MASCN on PSS films highlighting that the build-up of I_3^- is not observed when MAI is combined with a SCN^- pseudohalogen.

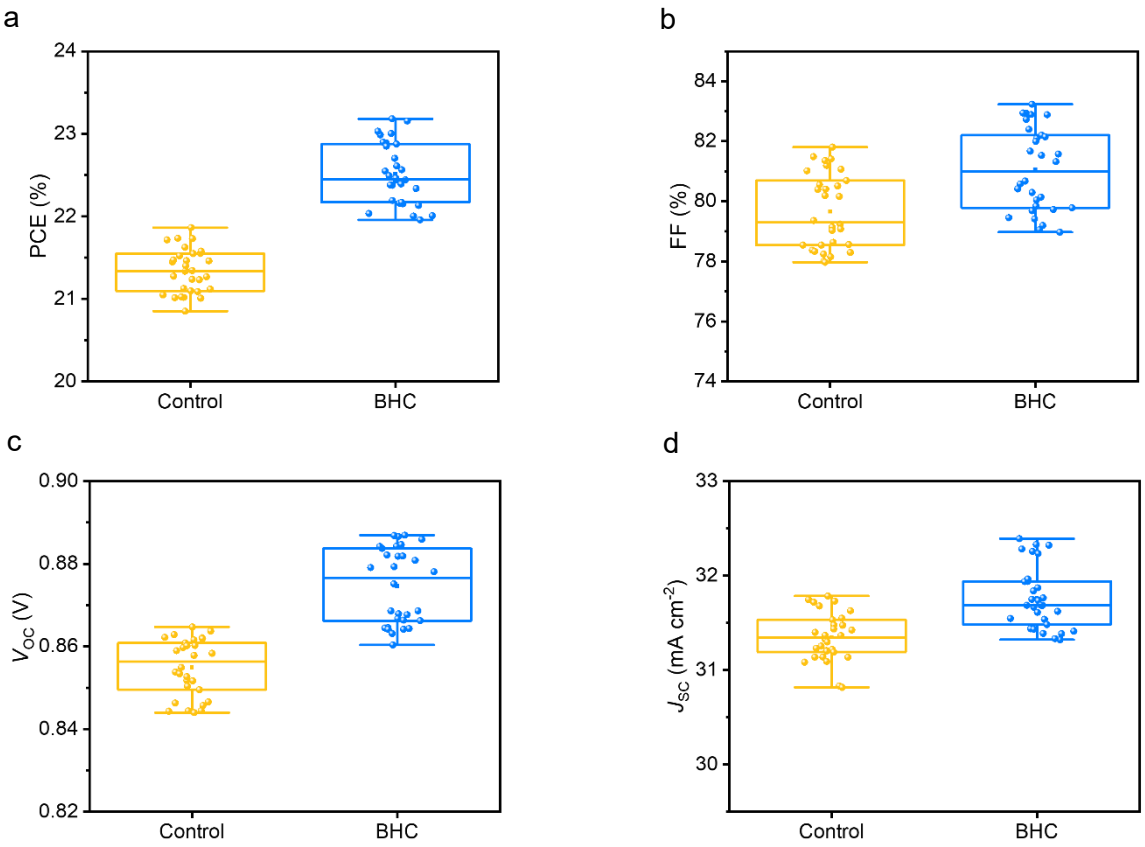

Supplementary Fig. 49. Statistical distribution of photovoltaic parameters for devices with and without BHC. Box plots for **a**, PCE, **b**, FF, **c**, V_{OC}, and **d**, J_{SC}.

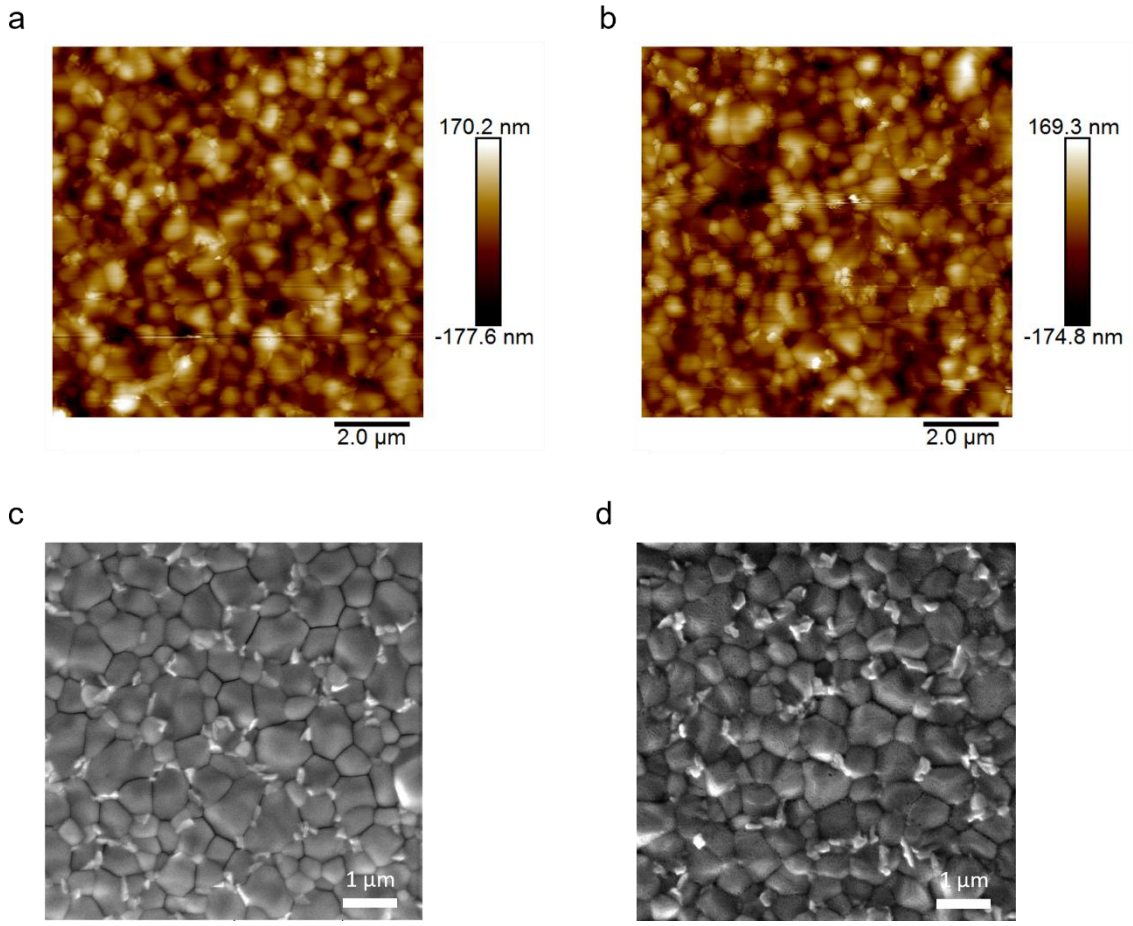

Supplementary Fig. 50. Microstructure of Pb-Sn perovskite films with and without BHC. AFM height image of **a.** Control film (without BHC), and **b.** BHC incorporated perovskite film. Both samples indicate a similar root mean square roughness of ~49 nm. SEM image of **c.** Control film (without BHC), and **d.** BHC incorporated perovskite film.

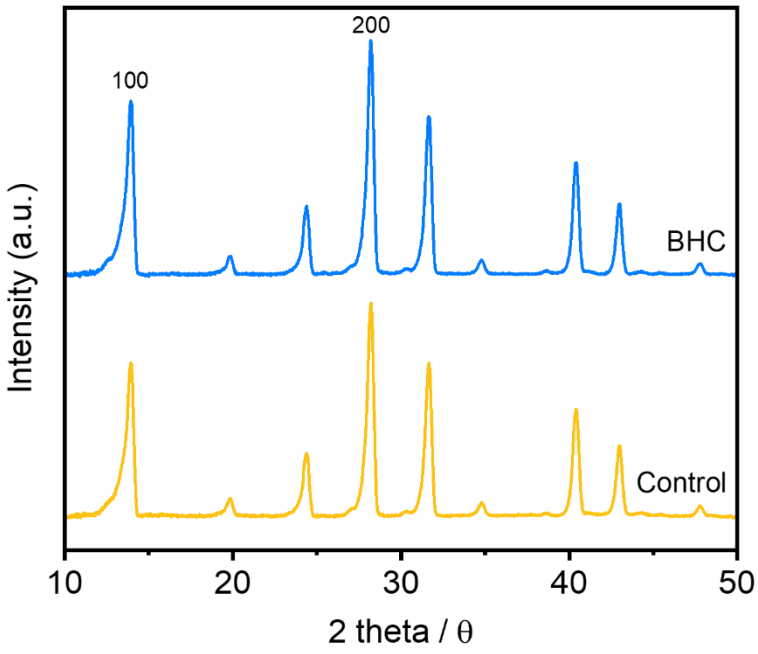

Supplementary Fig. 51. GIXRD spectra of Pb-Sn perovskite films with and without BHC, acquired at an incident angle of 1°.

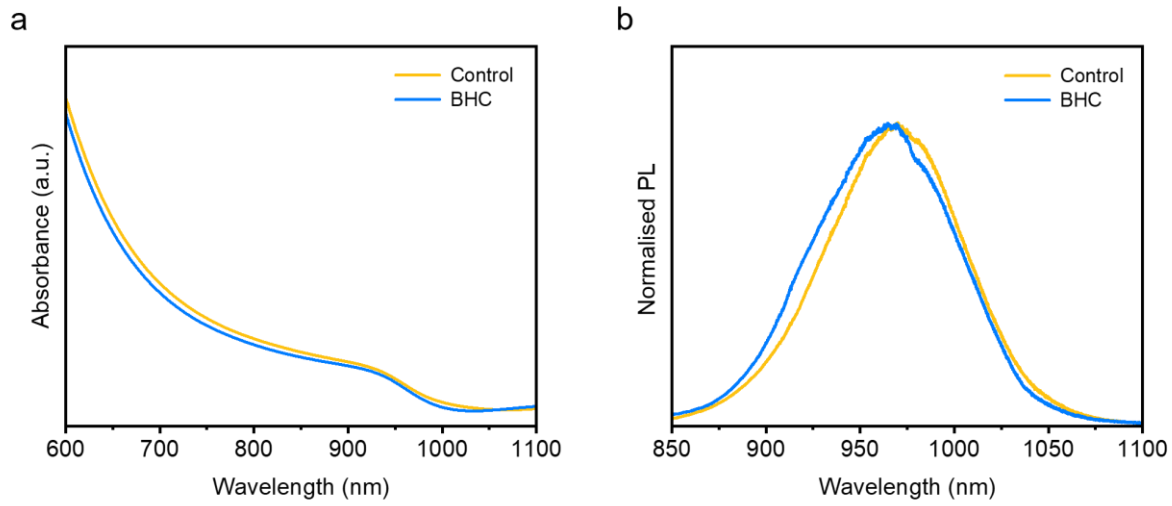

Supplementary Fig. 52. Optoelectronic properties of Pb-Sn perovskite films with and without BHC. **a.** UV-Vis absorbance spectra, and **b.** Normalised photoluminescence (PL) spectra of the films.

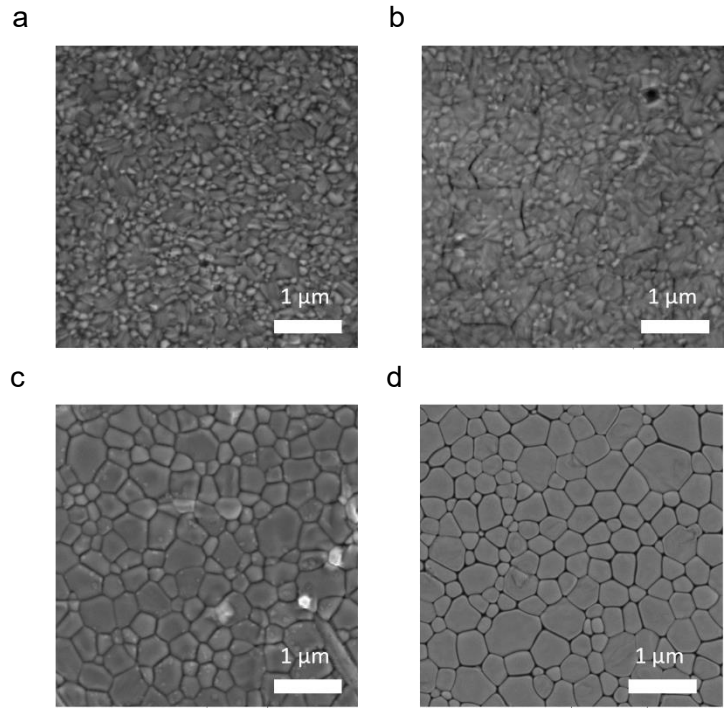

Supplementary Fig. 53. Microstructure of PEDOT:PSS/MAPI films with additional MAI subjected to modified annealing treatment. The SEM micrographs are given for **a**, regular annealing in glove box, **b**, regular annealing in glove box with excess MAI incorporated to the perovskite, **c**, prolonged annealing, and **d**, solvent vapor annealing in air.

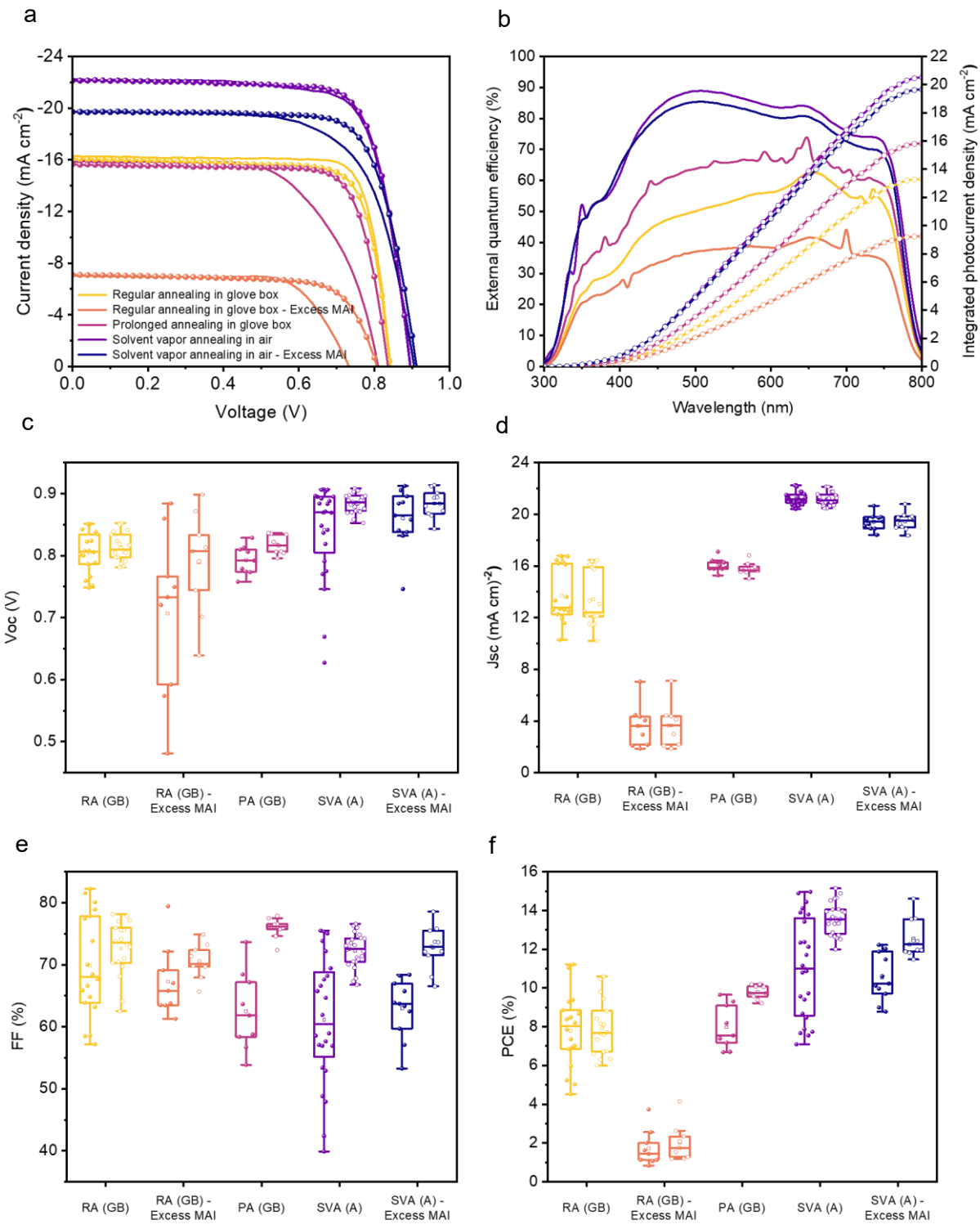

Supplementary Fig. 54. Device performance characteristics PEDOT:PSS/MAPI films with additional MAI subjected to modified annealing treatment. **a**, *J-V* curves of champion devices in both forward (line) and reverse (line + symbol) directions. **b**, Corresponding EQE spectra and integrated J_{SC}. Box plots for **c**, V_{OC}, **d**, J_{SC}, **e**, FF, and **f**, PCE.

Supplementary Note 1: Transient Absorption Spectroscopic Analysis

Transient absorption (TA) spectroscopy is used to follow the carrier dynamics. **Supplementary Fig. 5a–c** and **d–f** show the TA maps and spectra respectively of PEDOT:PSS/MAPI, PEDOT:PSS/MAPI+SCN^-, and PTAA/MAPI under a 400-nm pump with fluence of ~2.3 μJ cm^{-2} (incident from the perovskite layer), corresponding to an injected carrier density of 1.06×10^{17} cm^{-3}. All samples give a ground state bleach (GSB) centered at ~760 nm with a full width at half maximum of ~75 meV, corresponding to the energy of direct band-to-band transition of MAPI perovskites.

Supplementary Fig. 5g shows the kinetics of the GSB signals for PEDOT:PSS/MAPI (in blue), PEDOT:PSS/MAPI+SCN^- (in yellow) and PTAA/MAPI (in red) samples. The longest decay components for the samples are 817 ns, 1854 ns and 9551 ns, respectively, fit by mono-exponential decay of the signals after 350 ns. This corresponds to mono-exponential recombination due to traps (i.e., Shockley-Read-Hall recombination) in three-dimensional perovskites with a rate constant of 1.22×10^6 s^{-1} for PEDOT:PSS, 5.40×10^5 s^{-1} for PEDOT:PSS when SCN is incorporated to the perovskite, and 1.05×10^5 s^{-1} for PTAA. The relatively smaller rate constant for MAPI+SCN^- on PEDOT:PSS as compared to pristine MAPI on PEDOT:PSS indicates a low density of trap states with the addition of SCN^-, and the PTAA/MAPI sample with the smallest rate constant shows the least non-radiative energy loss among all samples.

Supplementary Note 2: Time and Frequency Domain analysis

Analysis of the rise and decay characteristics (**Supplementary Fig. 6a** and **b**) of transient photocurrent (TPC) measurements shows that among the device stacks studied here, PTAA results in the fastest transients indicative of the least charge trapping effects while PEDOT:PSS devices in the absence of SCN^- results in the longest rise as well as decay transients. The incorporation of SCN^- into the bulk of the perovskite leads to an intermediate behaviour in agreement with the trends observed from TAS.

An intriguing feature observed within the TPC characteristics is the lack of saturation in the photocurrent (**Supplementary Fig. 6c**), a feature commonly observed in devices operating in the photo-conducting gain mode[14]. To identify whether such a transient behaviour is due to mobile ions within the device, we conducted Intensity Modulated Photocurrent Spectroscopy (IMPS) (**Supplementary Fig. 6d**). From the PEDOT:PSS devices that does not contain SCN^-, we can observe a broad peak in the frequency range of 10^0 – 10^3 Hz which is most likely due to a combination of ion migration effects and as a result of the formation of an extraction barrier, the origins of which are linked to the buried interface chemistry as will be discussed later on. At the high frequency end, we observe a more intense peak between 10^5 – 10^6 Hz and a shoulder (~10^3 – 10^5 Hz peak) which indicates an imbalance in terms of carrier transport in the bulk and extraction at the contacts and correlates with the slow transients observed in the TPC measurements. In comparison to the above, the inclusion of SCN^- leads to a loss of the shoulder peak while the effect of a signature of an extraction barrier and ion migration is also weakened. Both ion migration and charge extraction barriers are further suppressed when PTAA is used in place of PEDOT:PSS in line with the faster response and decay times as observed under TPC transients above.

Supplementary Note 3: Pathways for improved stability and efficiency

a) Improving efficiency in thiocyanate free devices by solvent vapor annealing

As discussed above, the addition of thiocyanates leads to improvements in the device performance characteristics driven by coarsening of the grains and reduced recombination processes. However, the thiocyanate also leads to a rapid degradation of the device. Therefore, an approach to generate larger grains in the absence of thiocyanate additives to yield better performances is desirable.

We utilised the solvent vapor annealing (SVA) assisted by dimethyl sulfoxide (DMSO) under a closed space as a strategy to restructure the perovskite half-cell (i.e. ITO/PEDOT:PSS/MAPI) and thereby to improve the device performance. Compared to the incorporation of thiocyanates, the SVA process leads to a more well-defined grain structure with an increase in the grain size following SVA (**Supplementary Fig. 53**). Following SVA, the thiocyanate free MAPI solar cells showed a PCE of ~15%– a nearly 50% improvement in PCE compared to the reference devices (**Supplementary Fig. 54**). The improvements in the PCE are observed to be driven by the high J_{SC} which increased from ~17 mA cm $^{-2}$ to ~22 mA cm $^{-2}$ following SVA (performance characteristics given in **Supplementary Fig. 54d**), approaching values realised on MAPI cells fabricated on PTAA and self-assembled monolayers. The V_{OC} also improved from ~0.84 V to ~ 0.90 V now. We further investigated the ISOS-D1 stability of unencapsulated devices under a relative humidity of 65% and observed sufficient device stability in line with PEDOT:PSS based devices that do not contain SCNs as discussed above. We note that increasing the annealing time alone for devices in the absence of a solvent induced restructuring does not lead to a similar level of performance gain. Further, the addition of excess MAI coupled with SVA whilst improving the performance compared to the reference devices, does not result in any further efficiency gains (**Supplementary Fig. 54f**). Evaluating the microstructure of films prepared with excess MAI also indicates a brighter topography compared to other structures fabricated and could potentially indicate the formation of a lead rich surface layer (**Supplementary Fig. 53**).

b) Optimisation of the Pb-Sn Device Architecture

Additive to the bulk for modulation of crystallisation: Thiocyanates in the form of either $Pb(SCN)_2$ or GASCN are employed in both narrow bandgap Pb-Sn, Sn-only and wide bandgap perovskites for achieving larger grain sizes[9,15,16]. Thoicyanates have been reported to hinder undesirable halide segregation in wide bandgap perovskites[17]. In addition to thiocyanates, FAH_2PO_2 and MAH_2PO_2 when added in controlled amounts to the precursor when high purity FAI and MAI are used, allows for increase in grain sizes. Alternately, careful regulation of the precursor concentration to increase absorber thickness in conjunction with additives has been reported to lead to larger grain sizes[18].

Within this study, as we used FAI and MAI without additional purification, the starting materials are likely to contain FAH_2PO_2 and MAH_2PO_2. Therefore, we followed the widely reported approach of retaining thiocyanates for modulation of the bulk crystallisation process allowing. We targeted the use of ammonium thiocyanate[7] in place of the more widely used to lead thiocyanate and guanidinium thiocyanate to mitigate undesirable degradation to the formation of excess lead halides and the potentially excessive de-doping of PEDOT:PSS with guanidinium cations even under low concentration.

Additive to inhibit oxidation of tin: We incorporated several strategies to inhibit the oxidation of Sn^{2+} to Sn^{4+}. Firstly, we included SnF_2, an additive that is widely recognised to mitigate the undesirable oxidation of Sn^{2+} and reduce the resulting high background carrier density[19–21]. We further incorporated glycine hydrochloride into the precursor mix. According to Hu et al.[7], the addition of glycine hydrochloride to the precursor leads to the formation of larger colloids which sediment early on resulting in the accumulation of glycine hydrochloride closer to the HTL/perovskite interface and leading the formation of larger perovskite grains. Building on this, Zhang et al. reported that the incorporation of glycine hydrochloride into the precursor also inhibits the oxidation of Sn^{2+} due to its antioxidant properties[22]. We further note that under neutral conditions (i.e. pH =7), glycine behaves as a zwitterion and as a result of its amphoteric behaviour[23], can passivate both halide and A-site vacancies[24,] both of which can occur as a result of the chemistry taking place at the buried interface. Finally following the work of Chen et al.[25], we incorporated benzyl hydrazine hydrochloride (BHC) at optimised concentrations to the precursor. Hydrazine and its derivatives are strong reducing agents and have the capability to scavenge iodine that is generated within the bulk. Iodine, in particular, has been previously reported by Lanzetta et al.[26]. as being a key driver for oxidation of Sn^{2+} and improves device lifetime. We further note that thiocyanates have also been reported to slow down the oxidation of Sn^{2+} [6]. Although the exact mechanism was not reported, based on the understanding developed within this study, it is reasonable to speculate that the interaction of SCN^- with iodine inhibits the oxidation of Sn^{2+}.

Replacing the BCP/Ag contact with ALD-SnO_2/Cu: The use of ALD-SnO_2 is known to act as a better barrier against moisture[26] and oxygen permeation to the device while Cu has better resistance to degradation that may take place due to mobile halide ions as opposed to the widely used Ag contacts. We note that further inhibition of contact degradation to ion migration can be realised through the incorporation of bismuth to form Bi/Cu bi-layered metallic contacts[6].

Additional note on the surface passivation agent: Within this study, we opted to use $EDAI_2$ as a surface passivation agent following the route first reported by Hu et al.[7] $EDAI_2$ is dissolved in a solvent mixture of 2-

propanol and toluene. Bandara et al. has previously reported that the use of toluene as an antisolvent leads to the removal of Sn^{4+} within the bulk of the perovskite[27] while a toluene wash of the crystallised perovskite film was reported as part of the processing route that led to fill factors approaching the Shockley Queisser limit for Pb-Sn perovskites as reported by Jayawardena et al.[28]. The underlying mechanism of Sn^{4+} removal with toluene was reported by Lanzetta et al.[29]. where this was used to obtain high quality SnI_2 material.

c) Alternate additives

Dewei Zhao and collaborators have previously reported in the use of cysteine hydrochloride in place of glycine hydrochloride for passivation of the bulk as well as the surface defects of Pb-Sn perovskites[30]. Cysteine forms sulfinic acids when with iodine[30] which in turn forms sulfates when moisture is present[31]. According to Yang et al.[32], sulfates can also be used for passivation of by interacting with Pb^{2+} cations at the surface through the following reaction:

$$\mathrm{APbX_3} + \mathrm{SO_4^{2-}} \rightarrow \mathrm{A^+} + 3\mathrm{X^-} + \mathrm{PbSO_4}$$

We also note that aminoiminomethanesulfinic, a zwitterionic additive used in Pb-Sn absorbers employed for record efficiency Pb-Sn perovskites when reacted with iodine, forms sulphates which can result in a similar passivation effect[33, 34]. This most likely explains in part, the high stability realised for devices that employ aminoiminomethanesulfinic acid as an additive.

Supplementary Note 4: Introduction of hydrazine derivatives to Pb-Sn perovskites

Among the numerous perovskite compositions that utilise SCN^-s, lead-tin mixed low band gap perovskites are the most dependant on PEDOT:PSS as an HTL, and SCN^- additives for improving device efficiency. Previously, we have shown that purification of the starting tin iodide powder[26] as well as solvent treatment during device fabrication[28] can mitigate the tin(iv) induced degradation of tin-based perovskite devices. However, the insights from this study point towards the clear need for mitigating the detrimental effects of iodine generated during the operation of the device. This is particularly important towards realising stable high efficiency all-perovskite multijunction devices as well as single junction, ideal band gap lead-tin or tin only PSCs.

Hydrazine derivatives have been identified as strong reducing agents for tin-based perovskite solar cells, where precursor and atmosphere-induced degradation has been mitigated through its addition[35,36]. In addition, the hydrazine-based additives have also been utilised for iodine management in perovskite precursors[25]. Based on this, we sought to investigate if the incorporation of hydrazine derivates can improve the stability of lead-tin mixed perovskites by scavenging of any iodine formed, thereby reducing the possibility of forming ICN, HCN and H_2SO_4 as discussed previously.

Supplementary Table 2. Examples of other iodine reductants and scavengers reported in the literature.

Device architecture	Reductant or scavenger	Ref
FTO/TiO_2/$MAPbI_3$/Spiro-OMeTAD/Au	PC60BM	[37]
FTO/PEDOT:PSS/$(FASnI_3)_{0.5}((MAPbI_3)_{0.5}$/PCBM/BCP/Ag	3-(3,4Dihydroxyphenyl)-DL-alanine (DOPA)	[13]
FTO/SnO_2/$Cs_{0.1}FA_{0.9}PbI_3$/Spiro-OMeTAD/Au	HCOOK	[38]
$Cs_{0.3-x}FAMA_xPb_{0.5}Sn_{0.5}I_3$ (x = 0, 0.15, 0.30)	CsI (post treatment)	[39]
$Cs_{0.3-x}FAMA_xPb_{0.5}Sn_{0.5}I_3$ (x = 0, 0.15, 0.30)	RbI (post treatment)	[39]
$Cs_{0.3-x}FAMA_xPb_{0.5}Sn_{0.5}I_3$ (x = 0, 0.15, 0.30)	$Na_2S_2O_3$ (post treatment)	[39]
ITO/PTAA/$MAPbI_3$ or $Cs_{0.1}FA_{0.9}PbI_{2.83}Br_{0.17}$/PFI/PCBM/C60/BCP/Cu	perfluorodecyl iodide (PFI)/PCBM/C60 stack on perovskite	[40]
ITO/PTAA/$MA_{0.7}FA_{0.3}PbI_3$/C60/BCP/Cu	$Zn(OOSCF_3)_2$	[41]
FTO/SnO_2/$FAPbI_3$/Spiro-OMeTAD/Au	mercaptoethylammonium iodide (ESAI)	[42]

References

1 L. Xu, Y. Li, C. Zhang, Y. Liu, C. Zheng, W. Lv, M. Li, Y. Chen, W. Huang and R. Chen, *Sol. Energy Mater. Sol. Cells*, 2020, **206**, 110316.

2 D. Li, T. Xia, W. Liu, G. Zheng, N. Tian, D. Yao, Y. Yang, H. Wang and F. Long, *Appl. Surf. Sci.*, 2022, **592**, 153206.

3 J.-J. Cao, Y.-H. Lou, W.-F. Yang, K.-L. Wang, Z.-H. Su, J. Chen, C.-H. Chen, C. Dong, X.-Y. Gao and Z.-K. Wang, *Chem. Eng. J.*, 2022, **433**, 133832.

4 H. Kim, Y. H. Lee, T. Lyu, J. H. Yoo, T. Park and J. H. Oh, *J. Mater. Chem. A*, 2018, **6**, 18173–18182.

5 D. B. Khadka, Y. Shirai, M. Yanagida and K. Miyano, *ACS Appl. Energy Mater.*, 2021, **4**, 12819–12826.

6 X. Hu, Y. Pan, J. Wang, Z. Liu and W. Chen, *Nano Energy*, 2023, **118**, 108937.

7 S. Hu, K. Otsuka, R. Murdey, T. Nakamura, M. A. Truong, T. Yamada, T. Handa, K. Matsuda, K. Nakano, A. Sato, K. Marumoto, K. Tajima, Y. Kanemitsu and A. Wakamiya, *Energy Environ. Sci.*, 2022, **15**, 2096–2107.

8 C. Li, Z. Song, C. Chen, C. Xiao, B. Subedi, S. P. Harvey, N. Shrestha, K. K. Subedi, L. Chen, D. Liu, Y. Li, Y.-W. Kim, C. Jiang, M. J. Heben, D. Zhao, R. J. Ellingson, N. J. Podraza, M. Al-Jassim and Y. Yan, *Nat. Energy*, 2020, **5**, 768–776.

9 J. Tong, Q. Jiang, A. J. Ferguson, A. F. Palmstrom, X. Wang, J. Hao, S. P. Dunfield, A. E. Louks, S. P. Harvey, C. Li, H. Lu, R. M. France, S. A. Johnson, F. Zhang, M. Yang, J. F. Geisz, M. D. McGehee, M. C. Beard, Y. Yan, D. Kuciauskas, J. J. Berry and K. Zhu, *Nat. Energy*, 2022, **7**, 642–651.

10 D. Zhao, Y. Yu, C. Wang, W. Liao, N. Shrestha, C. R. Grice, A. J. Cimaroli, L. Guan, R. J. Ellingson, K. Zhu, X. Zhao, R.-G. Xiong and Y. Yan, *Nat. Energy*, 2017, **2**, 17018.

11 L. Huang, H. Cui, W. Zhang, D. Pu, G. Zeng, Y. Liu, S. Zhou, C. Wang, J. Zhou, C. Wang, H. Guan, W. Shen, G. Li, T. Wang, W. Zheng, G. Fang and W. Ke, *Adv. Mater.*, 2023, **35**, 2301125.

12 S. Hu, P. Zhao, K. Nakano, R. D. J. Oliver, J. Pascual, J. A. Smith, T. Yamada, M. A. Truong, R. Murdey, N. Shioya, T. Hasegawa, M. Ehara, M. B. Johnston, K. Tajima, Y. Kanemitsu, H. J. Snaith and A. Wakamiya, *Adv. Mater.*, 2023, **35**, 2208320.

13 Y. Xing, Z. Deng, T. Guo, Z. Zhang, Q. Tai, R. Zhao, J. Xiong, Q. Wang, L. Huang, X. Liu, Z. Hu, Y. Zhu and J. Zhang, *Chem. Eng. J.*, 2023, **462**, 142122.

14 H. M. Thirimanne, K. D. G. I. Jayawardena, A. J. Parnell, R. M. I. Bandara, A. Karalasingam, S. Pani, J. E. Huerdler, D. G. Lidzey, S. F. Tedde, A. Nisbet, C. A. Mills and S. R. P. Silva, *Nat. Commun.*, 2018, **9**, 2926.

15 M. A. Mahmud, J. Zheng, S. Tang, C. Liao, G. Wang, J. Bing, T. L. Leung, A. D. Bui, H. Chen, J. Yi, S. P. Bremner, H. T. Nguyen and A. W. Y. Ho-Baillie, *ACS Energy Lett.*, 2023, **8**, 21–30.

16 J. Tong, Z. Song, D. H. Kim, X. Chen, C. Chen, A. F. Palmstrom, P. F. Ndione, M. O. Reese, S. P. Dunfield, O. G. Reid, J. Liu, F. Zhang, S. P. Harvey, Z. Li, S. T. Christensen, G. Teeter, D. Zhao, M. M. Al-Jassim, M. F. A. M. Van Hest, M. C. Beard, S. E. Shaheen, J. J. Berry, Y. Yan and K. Zhu, *Science*, 2019, **364**, 475–479.

17 S. Martani, Y. Zhou, I. Poli, E. Aktas, D. Meggiolaro, J. Jiménez-López, E. L. Wong, L. Gregori, M.

Prato, D. Di Girolamo, A. Abate, F. De Angelis and A. Petrozza, *ACS Energy Lett.*, 2023, **8**, 2801–2808.

18 R. Lin, J. Xu, M. Wei, Y. Wang, Z. Qin, Z. Liu, J. Wu, K. Xiao, B. Chen, S. M. Park, G. Chen, H. R. Atapattu, K. R. Graham, J. Xu, J. Zhu, L. Li, C. Zhang, E. H. Sargent and H. Tan, *Nature*, 2022, **603**, 73–78.

19 Q. Chen, J. Luo, R. He, H. Lai, S. Ren, Y. Jiang, Z. Wan, W. Wang, X. Hao, Y. Wang, J. Zhang, I. Constantinou, C. Wang, L. Wu, F. Fu and D. Zhao, *Adv. Energy Mater.*, 2021, **11**, 2101045.

20 K. J. Savill, A. M. Ulatowski, M. D. Farrar, M. B. Johnston, H. J. Snaith and L. M. Herz, *Adv. Funct. Mater.*, 2020, **30**, 2005594.

21 I. Chung, B. Lee, J. He, R. P. H. Chang and M. G. Kanatzidis, *Nature*, 2012, **485**, 486–489.

22 W. Zhang, L. Huang, H. Guan, W. Zheng, Z. Li, H. Cui, S. Zhou, J. Liang, G. Li, T. Wang, P. Qin, W. Ke and G. Fang, *Energy Environ. Sci.*, 2023, **16**, 5852–5862.

23 *Nature*, 1904, **69**, 545.

24 K. Xiao, R. Lin, Q. Han, Y. Hou, Z. Qin, H. T. Nguyen, J. Wen, M. Wei, V. Yeddu, M. I. Saidaminov, Y. Gao, X. Luo, Y. Wang, H. Gao, C. Zhang, J. Xu, J. Zhu, E. H. Sargent and H. Tan, *Nat. Energy*, 2020, **5**, 870–880.

25 S. Chen, X. Xiao, H. Gu and J. Huang, *Sci. Adv.*, 2021, **7**, eabe8130.

26 L. Lanzetta, T. Webb, N. Zibouche, X. Liang, D. Ding, G. Min, R. J. E. Westbrook, B. Gaggio, T. J. Macdonald, M. S. Islam and S. A. Haque, *Nat. Commun.*, 2021, **12**, 2853.

27 R. Lin, Y. Wang, Q. Lu, B. Tang, J. Li, H. Gao, Y. Gao, H. Li, C. Ding, J. Wen, P. Wu, C. Liu, S. Zhao, K. Xiao, Z. Liu, C. Ma, Y. Deng, L. Li, F. Fan and H. Tan, *Nature*, 2023, **620**, 994–1000.

28 R. M. I. Bandara, K. D. G. I. Jayawardena, S. O. Adeyemo, S. J. Hinder, J. A. Smith, H. M. Thirimanne, N. C. Wong, F. M. Amin, B. G. Freestone, A. J. Parnell, D. G. Lidzey, H. J. Joyce, R. A. Sporea and S. R. P. Silva, *J. Mater. Chem. C*, 2019, **7**, 8389–8397.

29 A. Wijesekara, Y. Han, D. Walker, S. Huband and R. Hatton, *Adv. Sci.*, 2023, **10**, 2301497.

30 J. Luo, R. He, H. Lai, C. Chen, J. Zhu, Y. Xu, F. Yao, T. Ma, Y. Luo, Z. Yi, Y. Jiang, Z. Gao, J. Wang, W. Wang, H. Huang, Y. Wang, S. Ren, Q. Lin, C. Wang, F. Fu and D. Zhao, *Adv. Mater.*, 2023, **35**, 2300352.

31 S. V Makarov, C. Mundoma, J. H. Penn, S. A. Svarovsky and R. H. Simoyi, *J. Phys. Chem. A*, 1998, **102**, 6786–6792.

32 S. Yang, S. Chen, E. Mosconi, Y. Fang, X. Xiao, C. Wang, Y. Zhou, Z. Yu, J. Zhao, Y. Gao, F. De Angelis and J. Huang, *Science*, 2019, **365**, 473–478.

33 W. Wei, J. Wen, D. Yang, H. Jing, J. You and H. Wang, *RSC Adv.*, 2015, **5**, 4416–4419.

34 E. Mambo and R. H. Simoyi, *J. Phys. Chem.*, 1993, **97**, 13662–13667.

35 X. Dai, S. Chen, H. Jiao, L. Zhao, K. Wang, Z. Ni, Z. Yu, B. Chen, Y. Gao and J. Huang, *Nat. Energy*, 2022, **7**, 923–931.

36 T.-B. Song, T. Yokoyama, C. C. Stoumpos, J. Logsdon, D. H. Cao, M. R. Wasielewski, S. Aramaki and M. G. Kanatzidis, *J. Am. Chem. Soc.*, 2017, **139**, 836–842.

37 J. Xu, A. Buin, A. H. Ip, W. Li, O. Voznyy, R. Comin, M. Yuan, S. Jeon, Z. Ning, J. J. McDowell, P. Kanjanaboos, J. P. Sun, X. Lan, L. N. Quan, D. H. Kim, I. G. Hill, P. Maksymovych and E. H. Sargent, *Nat. Commun.*, 2015, **6**, 1–8.

38 D. Sun, Y. Gao, H. Raza, S. Liu, F. Ren, X. Hu, H. Wang, X. Meng, J. Wang, R. Chen, H. Sun, J. He, J. Zhou, Y. Pan, Z. Sun, W. Chen and Z. Liu, *Adv. Funct. Mater.*, 2023, **33**, 2303225.

39 A. Alsulami, L. Lanzetta, L. Huerta Hernandez, D. Rosas Villalva, A. Sharma, S. P. Gonzalez Lopez, A.-H. Emwas, A. Yazmaciyan, F. Laquai, I. Yavuz and D. Baran, *J. Am. Chem. Soc.*, 2024, **146**, 22970–22981.

40 X. Ren, J. Wang, Y. Lin, Y. Wang, H. Xie, H. Huang, B. Yang, Y. Yan, Y. Gao, J. He, J. Huang and Y. Yuan, *Nat. Mater.*, 2024, **23**, 810–817.

41 M. A. Uddin, P. J. S. Rana, Z. Ni, G. Yang, M. Li, M. Wang, H. Gu, H. Zhang, B. D. Dou and J. Huang, *Nat. Commun.*, 2024, **15**, 1355.

42 X. Lu, K. Sun, Y. Wang, C. Liu, Y. Meng, X. Lang, C. Xiao, R. Tian, Z. Song, Z. Zhu, M. Yang, Y. Bai and Z. Ge, *Adv. Mater.*, 2024, **36**, 2400852.